Quantum Optics and Photonics

Academic and Research Staff
Prof. Shaoul Ezekiel, Dr. Selim M. Shahriar, Dr. Byoung Ham, Dr. A. Kumarakrishnan, Dr. V. S. Sudarshanam, Dr. Alexey Turukhin, Dr. Parminder Bhatia, Juanita Riccobono

Visiting Scientist and Research Affiliates
Prof. Jeffrey Shapiro, Prof. Seth Lloyd, Prof. Cardinal Warde, Prof. Mara G. Prentiss, Prof. Marc Cronin-Golomb, Dr. Susanne Yelin, Dr. Misha Lukin, John D. Kierstead, Etsuko Nomoto

Graduate Students
Ying Tan, Jacob Morzinski, Brian Demsky, Thomas Liptay, Niell Elvin, Ward Weathers

Undergraduate Students
Tanya Zelevinsky, Aaron VanDevender, Shome Basu, Edward Flagg

Website: http://qop.mit.edu/

1. Experimental Progress Towards a Many-Bit Quantum Computer: Observation and Study of Raman Excited Spin Alignment in NV-Diamond

Sponsors: AFOSR grant #F49620-98-1-0313, ARO grant # DAAG55-98-1-0375, and the Hertz Foundation

We have been pursuing the use of NV color centers in diamond for realizing a many-bit quantum computer, as well as for a high-capacity data storage system. For both of these applications, the first critical step is the creation of coherent spin alignment using two-photon optical (Raman) transitions. Here, we report on our recent observation of this process, and the studies we have conducted to characterize it.

Recent developments in the field of quantum information and quantum computing has stimulated an intensive search for coherent physical processes which could be used to manipulate coupled quantum systems in a controlled fashion[1]. In this section, we describe our preliminary results demonstrating Raman excited spin alignment in NV-diamond, and its implication for the coherent generation and manipulation of entangled metastable states of interacting pairs of atoms. Entanglements created this way can in turn be used to realize a quantum computer with hundreds of bits.

We have previously reported in detail on our approach for realizing a quantum computer using a spectral-hole-burning solid[2]. Briefly, in our model a high-finesse optical cavity operating in the strong coupling regime is used to produce, via a two-photon transition, effective dipole-dipole coupling between two color centers that are spectrally adjacent. Recently, we have developed a variant of this approach using direct dipole-dipole interaction, also controlled by a two-photon transition. This model is presented in greater detail in section 7. The experimental parameters of NV-diamond makes it a suitable candidate for realizing either of these approaches for quantum computing.

NV-diamond can be used also for high-temperature hole-burning memories. Optical spectral hole-burning has demonstrated the ability to achieve high-capacity, high-speed data storage[3]. The biggest stumbling block to its widespread application has been the requirement for low temperature operation and the associated costs thereof. To circumvent this problem, we have been investigating the possibility of using Raman excited spin coherences to store and recall optical data. The motivation is that optical Raman excitation allows storage densities and response times characteristic of optical hole-burning memories, but since it is based on long-lived spin coherences, it can maintain these characteristics at much higher operating temperatures.

Proof-of-principle experiments have shown the ability to store and recall optical data using Raman excited spin echoes in Pr:YSO. The potential for higher temperature operation, without loss of performance, was also demonstrated in this material. Recently, we have shown that it is possible to observe Raman dark resonances above the spectral hole burning temperature in Pr:YSO. However, to achieve much higher temperature operation, a spectral hole-burning material with an allowed optical transition is required. This is necessary to offset the loss of efficiency of the Raman interaction, due to increasing optical homogeneous width as temperature is increased. NV color centers in diamond is such a medium, and can be used to realize a ultra-high capacity, high temperature as the Raman hole-burning material because it is comparatively well studied[4].

The experimental setup used in the N-V diamond studies is shown in Figure 1. Here, a Raman enhanced non-degenerate four-wave mixing (NDFWM) technique is used to achieve a high signal to noise ratio, in analogy to experimental techniques used previously to study Pr:YSO [5]. In this scheme, coupling (C) and probe (P) field are used to write a grating in the ground state spin coherence via the resonance Raman interaction. This grating is read with a read beam (R) to produce a signal or diffracted beam (D). To further enhance signal to noise, a heterodyne detection scheme is used as shown in Figure 1(b). All dye laser beams are derived from a single dye laser output using acousto-optic frequency shifters. This greatly relaxes dye laser frequency stability requirements since the resonant Raman interaction is insensitive to correlated laser jitter. An additional beam from the argon laser (A) is also directed into the sample to serve as a repump. Without this repump beam, the N-V center would exhibit long-lived spectral hole-burning and no cw signal would be seen after a short time. The Raman transition frequency (~120 MHz) is determined by the spacing between the S=0 and S=-1 ground state spin sublevels. This spacing is controlled by applying a magnetic field of about 1 kGauss along the crystal (111) direction. At this field strength, the S=0 and S=-1 ground sublevels (for N-V centers aligned along (111)) are near an anti-crossing. These conditions are chosen to enhance Raman transition strength by compensating for the small spin-orbit coupling in diamond with a partial mixing the spin sublevels[4].

The observed NDFWM signal is shown in Figure 2 as a function of Raman detuning. The amplitude of this signal is directly proportional to the degree of coherent spin alignment induced in the NV color centers. For convenience, the Raman detuning is adjusted by tuning the spacing between the S=0 and S=-1 sublevels using the applied magnetic field. As shown, the Raman linewidth is about 20 MHz, which is comparable to the 15 MHz inhomogeneous width of the ground state spin transition. This width is significantly smaller than the homogeneous width (>>25 MHz) of the optical transition and laser jitter (~100 MHz), and is taken as evidence of the Raman process. The asymmetry in the lineshape is due to interference with the (much broader) NDFWM signal at the anti-crossing. To eliminate this interference and to improve quality of the NDFWM signal, scanning of probe beam frequency is required. This was achieved by introducing electro-mechanical galvos. Compensating of angular displacement of coupling, probe, and reading beams, galvos allow scanning frequency of all beams. To further expand capability of the experimental setup, RF drivers for AOMs were configured to scan difference frequency between coupling and probe beam. A representative NDFWM signal obtained with modified setup is shown in Figure 3 as a function of frequency difference between coupling and probe beam. The value of the magnetic field was chosen about 1 kGauss and maintained constant.

Large optical matrix elements are required to maximize the number of gate operations per decoherence time. To evaluate matrix elements of our system, we investigated NDFWM diffraction amplitude as a function of laser intensity. The results are shown in Figure 4 for different laser intensities of coupling and probe beams. Intensity of the read beam was 25 W/cm^2, and intensity of the repump beam was around 10 W/cm^2. Saturation intensities were found to be 5 W/cm^2 and 3 W/cm^2 for coupling and probe transition respectively. Relatively high values of saturation intensities might be explained high optical density of this particular sample. Using obtained values of optical matrix elements, we can expect 100-1000 logic gate operations per spin decoherence time.

It is interesting to note that laser intensity has a great influence not only on amplitude of the NDFWM signal, but also on symmetry of lineshape. Figure 5 illustrates observed this dramatic change in lineshape.

Trying to optimize experimental conditions for observation of NDFWM signal, we studied NDFWM signal lineshape as a function of applied magnetic field. The experimental results are show in Figure 7. Sharp reduction in amplitude of the observed NDFWM signal far from central frequency most likely can be explained by limited bandwidth of the AOM used to scan the frequency of the probe beam. Further investigation of the obtained dependencies with proper renormalization of the signal is planed for the future.

Finally, Raman induced transparency of the probe field (P) has also been observed. Applying coupling laser power about 13 W/cm^2 , absorption suppression of the probe beam (1.3 W/cm^2) was evaluated to be about 4% (that corresponds change in transmission to be about 2.5%). Experimental traces are presented in Figure 8.

As a first step in investigation of spin echo in NV-diamond, we studied optical pumping effect on population of ground state. Regular NMR signal was detected at 430 MHz with applied magnetic field of 920 Gauss. RF power was modulated by square wave with frequency 50 Hz. Considering long lifetime of the metastable ground state, fall time of the observed pulses was strongly depended on efficiency of optical pumping. Experimental decay curve revealed two components: one weak component had constant fall time of about 5 ms, and the second stronger component had much shorter fall time, heavily depended on laser intensity. Therefore, weak component was attributed to unknown background signal, and the strong component was attributed to studied optical pumping effect. Experimental decay curves and corresponding fitting curves are shown in Figure 9.

To summarize, preliminary analysis of the NV-diamond shows a good potential of this material for experimental realization of solid state quantum computing based on dipole-dipole coupling. We have estimated that existing sample can provide as many as 900 coupled qubits per laser spot for quantum computing in spectrally selective solids. We have observed and studied Raman excited spin alignments. We have also analyzed the effects of laser power and magnetic field on Raman enhanced non-degenerate four-wave mixing signal. We have determined the optical matrix elements to be strong enough to allow 100-1000 logic gates operation per spin decoherence time.

References

1. C. Williams and S. Clearwater, Exploration in Quantum Computing (Springer-Verlag, New York, 1998).
2. M.S. Shahriar, J. Bowers, S. Lloyd, and P.R. Hemmer, “Solid State Quantum Computing Using Spectral Hole Burning,” submitted to *Nature* , and references therein.
3. H. Lin, T. Wang, and T. W. Mossberg, "Demonstration of 8-Gbit/in.2 areal storage density based on swept-carrier frequency-selective optical memory," *Optics Letters* **20**, pp. 1658-1660 (1995); X. A. Shen, E. Chiang, and R. Kachru, "Time-domain holographic image storage," *Optics Letters* **19**, pp. 1246-1248 (1994)
4. X.F. He, N.B. Manson, P.T.H. Fisk, “Paramagnetic resonance of photoexcited N-V defects in diamond. I. Level anticrossing in the ^{3}A ground state,” *Physical Review B* **47**, 8809 (1993); A. Lenef, S. W. Brown, D. A. Redman, S. C. Rand, J. Shigley and E. Fritsch, “Electronic structure of the N-*V* center in diamond: Experiments,” Physical Review B 53, 13427-13440 (1996).
5. B. S. Ham, M. S. Shahriar, M. K. Kim and P. R. Hemmer, "Frequency-selective time-domain optical data storage by electromagnetically induced transparency in a rare-earth-doped solid," *Optics Letters* **22**, pp. 1849-1851 (1997).

6. Solid State Quantum Computing Using Spectral Hole Burning," M.S. Shahriar, J. Bowers, S. Lloyd, and P.R. Hemmer, submitted to *Nature*

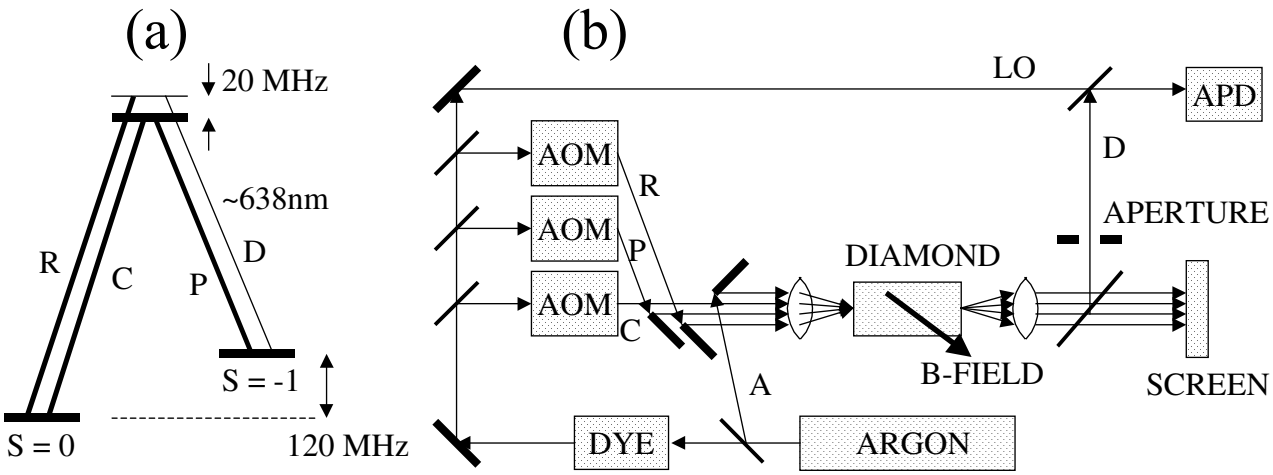

Figure 1. Experimental setup for observation of Raman excited spin coherences in N-V diamond. (a) Level diagram near anti-crossing. (b) Optical table setup.

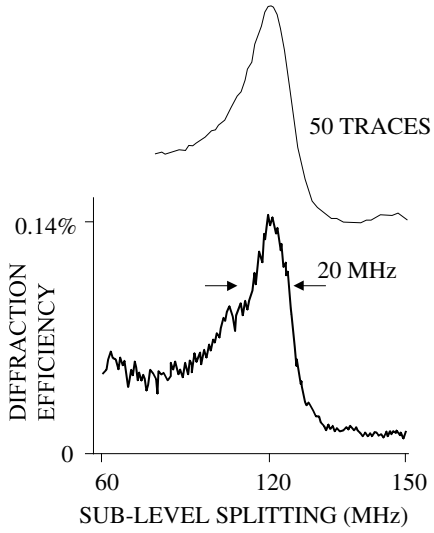

Figure 2. Raman enhanced non-degenerate four-wave mixing signal vs. magnetic field induced splitting of S=0,-1 states.

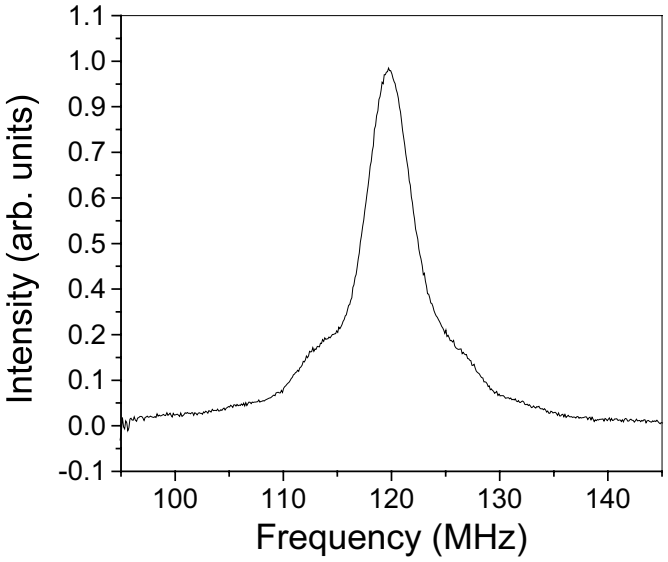

Figure 3. Raman enhanced non-degenerate four-wave mixing signal vs. frequency difference between coupling and probe beam.

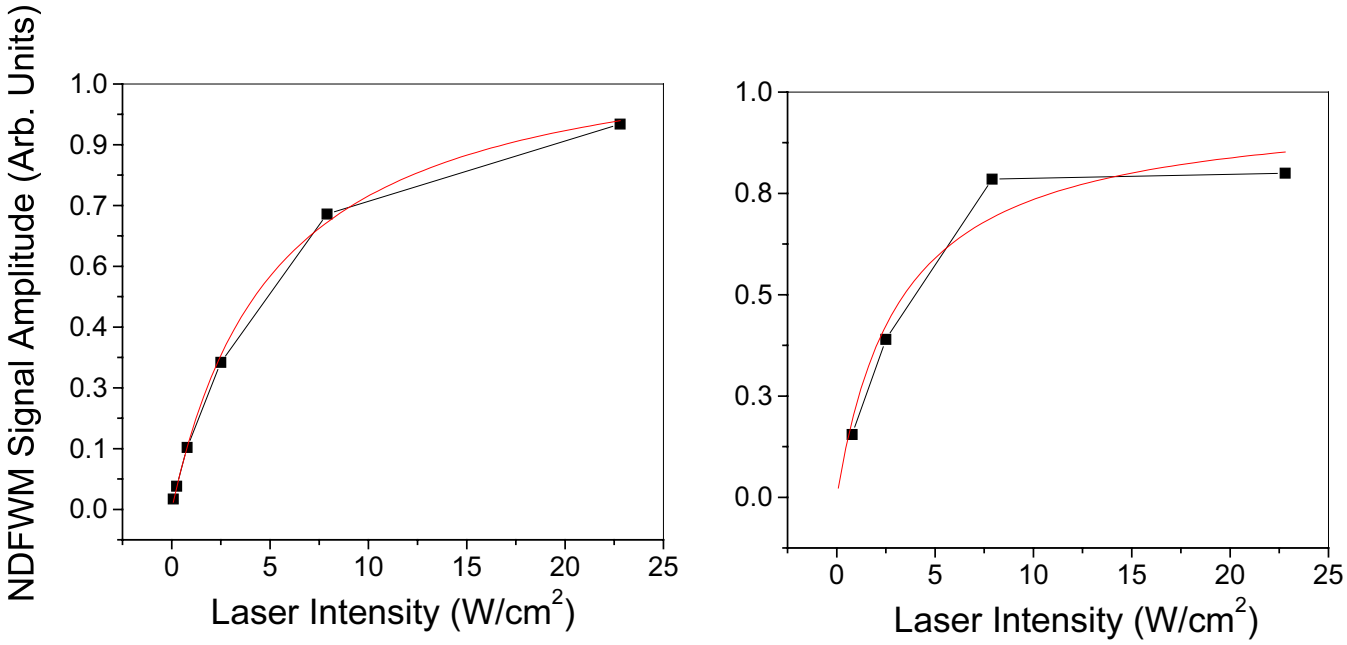

Figure 4. Amplitude of Raman enhanced non-degenerate four-wave mixing signal vs. laser intensity of coupling (left chart) and probe (right chart) beams.

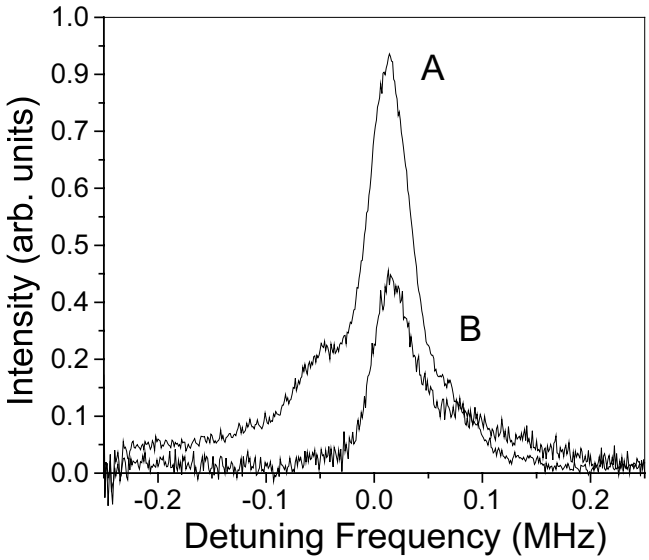

Figure 6. Observed raman enhanced non-degenerate four-wave mixing signal lineshape with applied full laser power (trace A) and 1/3 of full laser power (trace B).

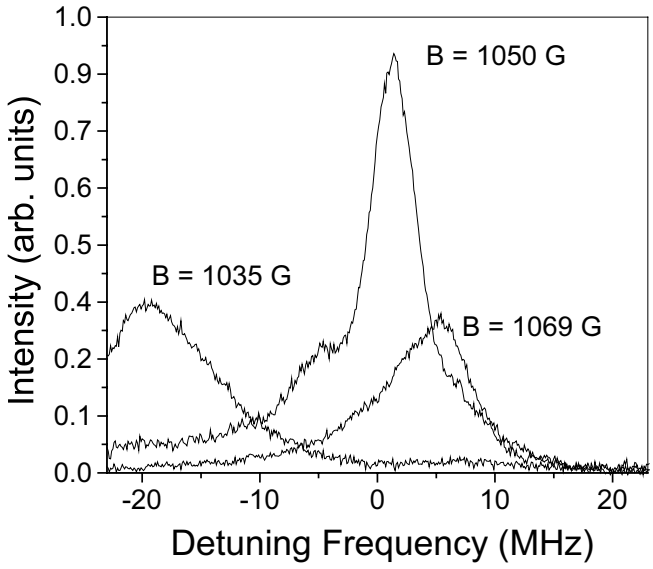

Figure 7. Raman enhanced non-degenerate four-wave mixing signal vs. magnetic field strength.

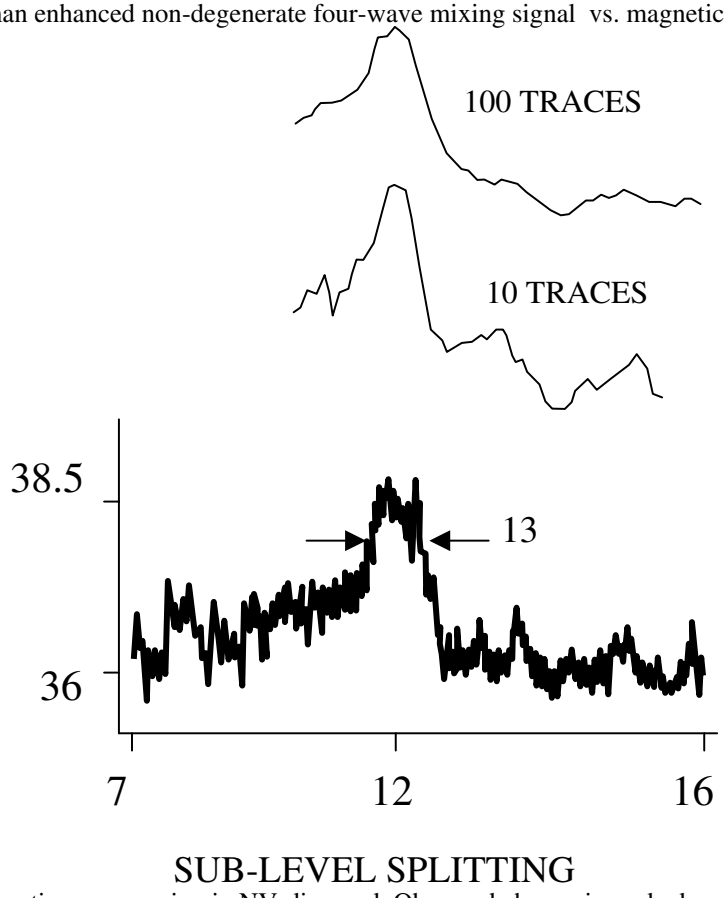

Figure 8. Absorption suppression in NV-diamond. Observed change in probe beam transmission is shown.

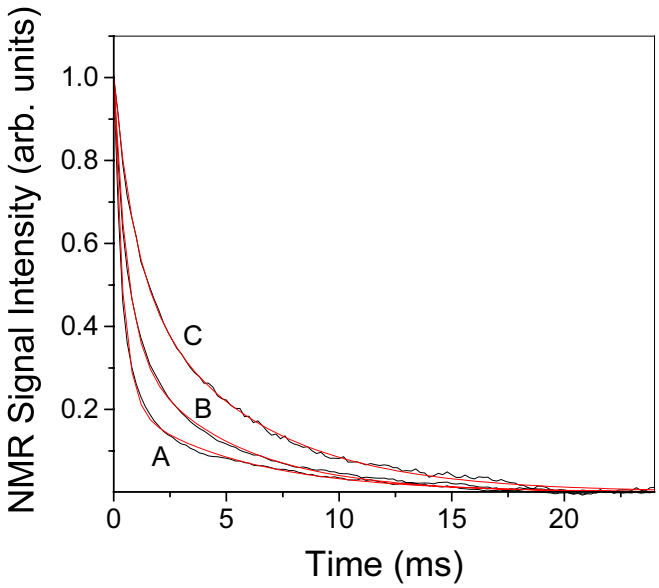

Figure 9. Ground state optical pumping after RF-pulse in NV-diamond. Optical pumping times of 0.40 ms, 0.58 ms, and 0.94 ms were found for laser powers of 96 mW/cm^2 , 48 mW/cm^2 , and 24 mW/cm

2. Demonstration of Injection-Locking a Diode Laser using a Filtered EOM Sideband

We have been pursuing the use of multi-pulsed Raman excitations for demonstrating a large area atom interferometer, using Rb atoms, in both one- and two-dimensions, with the dual goal of producing a ultra-precise rotation sensor, as well as to produce nanostructures with features as small as 4 nm. A key step in the experiment is the production of two laser frequencies that are phase coherent with each other to a few Hz. In this section, we report on realizing this goal, using a technique where an electro-optic modulator sideband is filtered through a cavity and injected into a diode laser, in a novel configuration yielding very high feedback isolation without sacrificing access to the output power of the diode laser. In section 3, we report on experimental results obtained using this system.

Many experiments in atomic physics require two laser beams with a controllable difference in frequencies. For frequency differences on the order of a few hundred MHz, an AOM can be used to directly produce a frequency shifted beam with high efficiency. However, AOMs that can shift a laser beam by a few GHz (e.g. 6.8 GHz for ^{87}Rb) have efficiencies close to one percent or less, and hence do not produce a frequency shifted beam with power that is adequate for some experiments.

For our large area atomic interferometer, initially using ^{85}Rb (and eventually ^{87}Rb for two-dimensions) we require two laser beams with frequencies separated by 3 GHz and with at least 50 mW of power each. An AOM or EOM can be used to produce a 3 GHz shift in frequency, but neither will produce a shifted beam with adequate power. (Both an AOM and an EOM only convert a few percent of the power in the original laser beam to the shifted frequency.) However, one can modelock a diode laser to the shifted beam produced by an AOM or EOM in order to increase the power of the frequency shifted beam. Modelocking involves sending a low power laser beam with a particular frequency into a diode laser. The diode laser lases at the frequency

of the low power beam. The final result is a sufficiently powerful laser beam shifted by 3 GHz from the original beam.

One of the drawbacks in using an AOM shifted beam is that the diffracted beam changes direction as the frequency is tuned. As a result, the diode lasers is not locked beyond a certain tuning range. Since many experiments, particularly ours, require the ability to tune the difference frequency by a significant amount, this misalignment imposes severe constraints, requiring additional compensation techniques. On the other hand, the sidebands produced by an EOM is always copropagating with the fundamental frequency, so that no such misalignment occurs as a result of tuning. As such, in principle, it is better to use an EOM for this approach. Furthermore, in general the frequency modulation achievable using an EOM is much higher than that achievable using an AOM. Finally, the EOM approach is analogous to yet another approach where the master laser is modulated directly; such an approach will eliminate the need for any external modulator, and as such is important for miniaturization efforts.

However, the EOM approach (and the direct modulation approach) has some obvious potential difficulties. First, the desired sideband needs to be filtered using a cavity with a high enough finesse so that the leakage from the fundamental is negligible. Second, the diode laser output may reflect back to itself from the surface of the cavity mirrors, causing instability. A simple isolation scheme often results in a configuration where only a part of the diode laser output is accessible for use as a single beam. Here, we report on our successful demonstration of realizing the EOM approach for locking a diode laser to a sideband of a Ti-Sapphire laser, shifted by ~3 GHz, using a novel isolation scheme that circumvents these problem.

A schematic of the setup that we used is shown in figure 1. First, a Ti-Sapphire laser beam is sent through an EOM driven by a 3 GHz microwave source, which in turn is phase locked to a rubidium atomic clock. The EOM outputs a laser beam with 3 frequency components: the original frequency, the original frequency + 3 GHz, and the original frequency – 3 GHz, which are all copropagating. The output beam is then sent through a Fabry Perot cavity in order to eliminate the original and downshifted frequencies from the beam. The cavity is first tuned to the transmission peak of the desired sideband, and then kept locked to this peak. The resulting output beam, upshifted by 3 GHz from the frequency of the Ti Sapphire beam, is then sent into a diode laser after passing through a polarizing beam splitter and a modified faraday isolator. The diode laser is injection-locked to this upshifted frequency, resulting in a 3 GHz upshifted beam with more than 100 mW of power, accessible in a single beam.

In order for the diode laser to modelock, the polarization of the diode laser beam must match the polarization of the upshifted beam being fed into it. Right before the diode laser beam enters the polarizing beam splitter it is horizontally polarized, whereas the upshifted Ti-Sapphire beam is vertically polarized at this point. In order to match the polarization of the upshifted beam to the diode laser beam, we placed a modified faraday isolator in the beam path. We explain later how the modified isolator works. Another challenge in the EOM setup is to prevent the diode laser from feeding back to itself. If even a few nanowatts of power from the diode laser are reflected back to the diode laser, then the diode laser becomes multimode and unstable.

In order to understand how the modified isolator works we will first recall how a normal isolator works and then discuss the modification we made to an isolator. A normal isolator consists of three basic pieces in series: a vertical polarizer, a material that rotates the polarization by 45 degrees, and a linear polarizer oriented at 45 degrees. Figure 2a shows a picture of normal isolator with one beam entering from the right and one beam entering from the left. First, consider the beam entering from the left. The leftmost polarizer (vertically oriented) eliminates the horizontal component of the incoming beam while allowing the vertical component to continue. The beam, now vertically polarized, is then rotated by +45 degrees. Finally, the beam passes through a polarizer oriented at +45 degrees which does nothing to beams traveling from left to right since they are already polarized at +45 degrees. The net effect is that the vertical

component of the laser beam will pass through the isolator, but it will be rotated by 45 degrees at the output. The horizontal component of the same beam, on the other hand, will not pass through the vertical polarizer and hence will not make it through the isolator. Next, consider the beam entering the isolator from the right hand side. No matter how the beam is oriented, after it passes through the first polarizer it encounters, its will become polarized in the direction of the polarizer, +45 degrees. This polarization will then be rotated by +45 degrees resulting in a horizontally polarized beam. Since the final polarizer is oriented vertically and the beam is horizontally polarized, none of the beam power will pass through the polarizer. Hence, regardless of polarization, no beam will be able to pass through the isolator from the right.

Our modified isolator is just like a normal isolator only without the linear polarizer oriented at 45 degrees. (See figure 2b) This modification does not affect beams passing through the isolator from left to right since they are already polarized at +45 degrees by the time they reach the +45 degree polarizer. However, beams traveling from the right can now pass through the isolator. For example, a beam oriented at –45 degrees and traveling from right to left will not be attenuated by the isolator at all. It's polarization will be rotated by +45 degrees, so that it becomes vertically polarized. Then it will pass through the vertical polarizer unattenuated. Thus, the only change to a beam oriented at –45 degrees traveling from right to left, will be that its polarization is rotated by +45 degrees so that it is vertically polarized upon exiting the isolator.

The diode laser beam is initially vertically polarized. It passes through the modified isolator with no power loss, but is rotated by +45 degrees. A half wave plate then rotates the beam by another +45 degrees so that the diode laser beam is horizontal before entering the polarizing beam splitter. The diode laser continues through the polarizing splitter, which only reflects vertically polarized light, to the experiment. The Ti-Sapphire laser is initially circularly polarized. After passing through the EOM and the Fabry Perot cavity the beam is upshifted by 3 GHz, but has only about 4% of its original power. The beam then passes through a quarter wave plate that changes the polarization from circular to vertical. After being reflected by the polarizing beam splitter, the upshifted beam passes through the half-wave plate and becomes polarized at –45 degrees. The beam continues through the modified isolator to the diode laser. Note that we use the modified isolator to convert cross polarized beams to beams with parallel polarizations. Without the modified isolator the polarizations of the diode laser beam and the Ti-Sapphire beam would not match at the diode laser and hence injection locking would not occur.

If optical components were ideal then there would be no feedback to the diode laser under this configuration. However, we found that enough residual light was still feeding back to the diode laser upon reflection from the FP cavity to cause multimode behavior. In order to combat this unwanted residual feedback, we put a quarter wave plate between the polarizing beam splitter and the FP cavity. This quarter wave plate is oriented so that vertically polarized diode laser light that is reflected by the polarizing beam splitter becomes circularly polarized after passing through it. Any of the diode light that reflects back from the Fabry Perot cavity, passes through the quarter wave plate a second time and is converted from circularly polarized to horizontally polarized. Since almost all of the diode light reflected by the polarizing beam splitter is horizontally polarized after passing through the quarter wave plate, reflecting off of the Fabry perot cavity, and then passing through the quarter wave plate again, almost all of the light passes straight through the polarizing beam splitter and is prevented from feeding back to the diode laser.

Thus, our setup effectively filters the reflected diode laser beam twice. When the main diode laser beam is sent through the polarizing beam splitter only a small fraction of the beam δ is reflected. Part of the reflected beam then reflects off of the Fabry Perot cavity and returns to the polarizing beam splitter. Again only a small fraction of this light δ is reflected back towards the diode laser. In the end a maximum of δ^2 fraction of the diode laser beam feeds back to the diode laser.

In order to test the degree to which the diode laser is phase-locked to the sideband from the T-Sapph laser, we sampled a part of the injection beam, and shifted it by a 270 MHz AOM. This beam was then combined with a sample from the diode laser output, and the beat note was detected using an APD detector. Figure 3 shows this beatnote, with a width of about 2 KHz, which is essentially the resolution limit of the spectrum analyzer. Fundamentally, we expect the beat-note to be very narrow (perhaps a few Hz), limited only by the noise in the servo used to phase lock the 3 GHz VCO to the rubidium clock.

As reported in section 3, we have used this injection locking scheme to observe Raman-Ramsey fringes with an width (~1 kHz) that is very close to the transit time limited value, including some residual broadening from the longitudinal velocity spread. Assuming that the linewidth of the Raman-Ramsey fringes results from the convolution of the this theoretical width and any residual width of the beat-note, we can infer that the beat-note is less than 100 Hz. When we repeat this experiment using trapped atoms, which will yield a much narrower (~1 Hz) transit-time limited linewidth, we would be able to determine the beat-note with better precision.

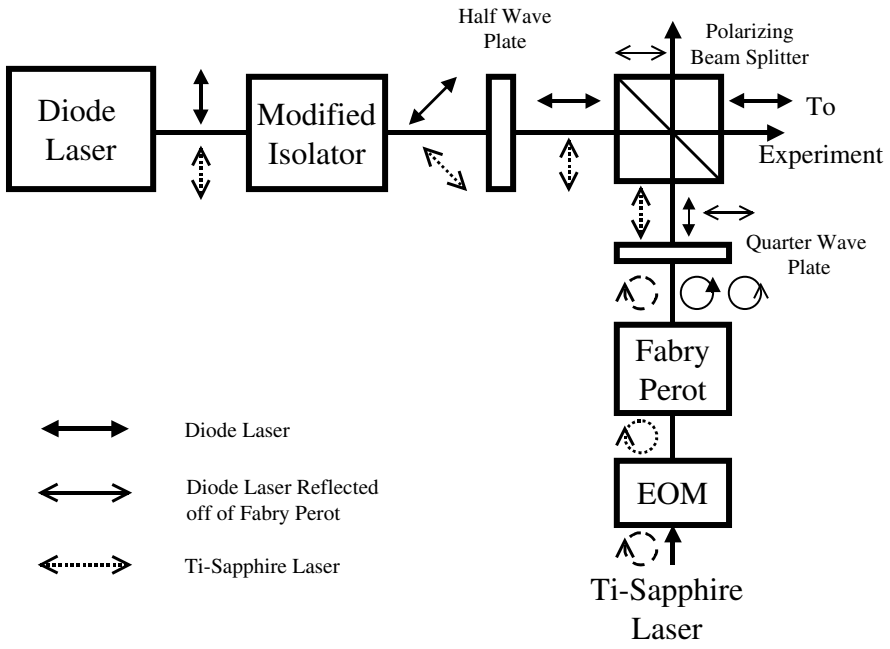

Figure 1: A schematic of the setup we use to modelock a diode laser to a frequency shifted Ti-Sapphire laser beam. An EOM upshifts part of the Ti-Sapphire beam by 3 GHz. A Fabry Perot cavity is then used to eliminate all frequencies from the beam except for the part upshifted by 3 GHz. After passing through polarizing beam splitter the polarization of the upshifted beam is rotated 90 degrees by the modified isolator to match the polarization of the diode laser beam. The diode laser modelocks to the shifted beam, ie lases at the frequency of the upshifted beam. The main diode laser beam passes straight through the polarizing beam splitter and goes to the experiment. However, because the optical components are not ideal the polarizing beam splitter reflects a fraction of the diode laser light. Some of this reflected light reflects off of the Fabry Perot cavity and returns to the polarizing beam splitter. Since the quarter wave plate makes the reflected diode laser light horizontally polarized, only a small amount of diode laser light reflected off of the Fabry Perot cavity returns to the diode laser.

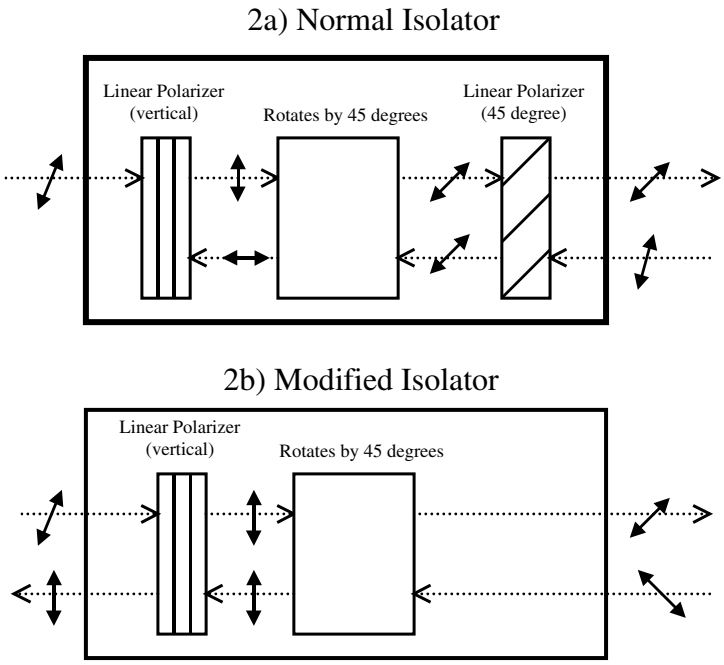

Figure 2: (a) Schematic illustration of a conventional faraday isolator. The vertical component of a laser beam traveling to the right passes through the isolator without any power loss, but is rotated by +45 degrees. However, no beam traveling to the left can pass through the isolator regardless of polarization. (b) Schematic illustration of our modified isolator. Our modification does not affect light traveling from right to left. However, it allows light traveling to the left and polarized at –45 degrees to pass through without any power loss. The modified isolator is useful because it allows us to convert beams which are cross polarized to beams with the same polarization.

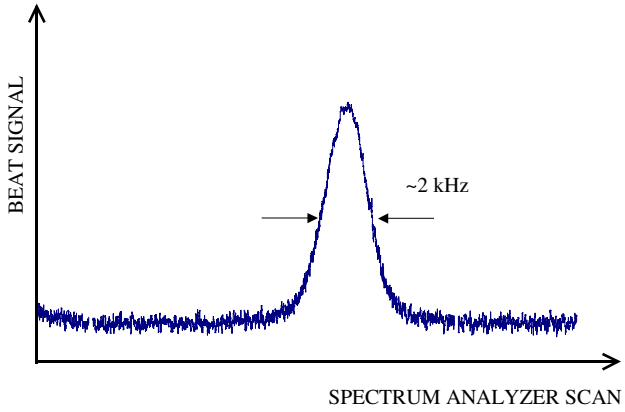

Figure 3: The beat note generated by mixing the injection locked diode laser with a beam from the Ti-Sapph laser. The beat note is centered around 270 MHz, corresponding to the frequency of the AOM used to shift the Ti-Sapph beam. The observed width of ~2kHz is limited by the resolution of the spectrum analyzer. The Raman-Ramsey fringes (shown in the next section) shows that the linewidth is at least less than 1 kHz.

3. Experimental Progress Towards Realization of a Large Area Atom Interferometer for Nanolithography: Observation of Transit-Time Limited Raman-Ramsey Fringes using Off-resonant Excitation in State-prepared ^{85}Rb

As mentioned in section 2, we have been investigating the use of off-resonant multi-pulse Raman excitations for creating a large area atom interferometer. Here, we report experimental progress towards this objective, using a thermal atomic beam of ^{85}Rb atoms, as well as trapped ^{85}Rb atoms. The combination of a Ti-Sapph laser and a diode laser injection locked to a sideband thereof, as discussed in section 2, was used as an essential tool in most of the results reported here.

The basic idea behind our scheme has been presented elsewhere, including the 1998 RLE progress report. Figure 1 shows schematically our experimental setup. The top shows the various frequency components that are necessary to realize our scheme in ^{85}Rb. Briefly, F_1 and F_2 are used for cooling the atomic beams in the two transverse directions. F_1 and F_5 are used to pump the populations in the Zeeman sublevels into a single, magnetic field insensitive sublevel. F_2 and F_3 are used to excite the Raman transition, either in an optically resonant mode or an optically off-resonant mode (as shown), for copropagating or counter-propagating configurations. The bottom shows schematically the explicit arrangement of the various optical beams with reference to the atomic beam apparatus.

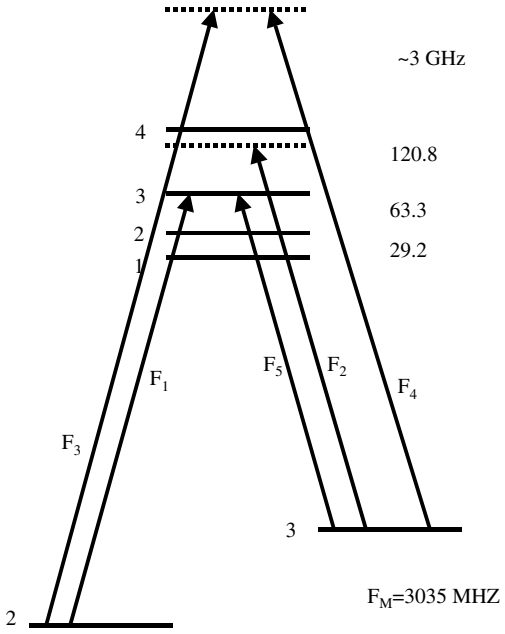

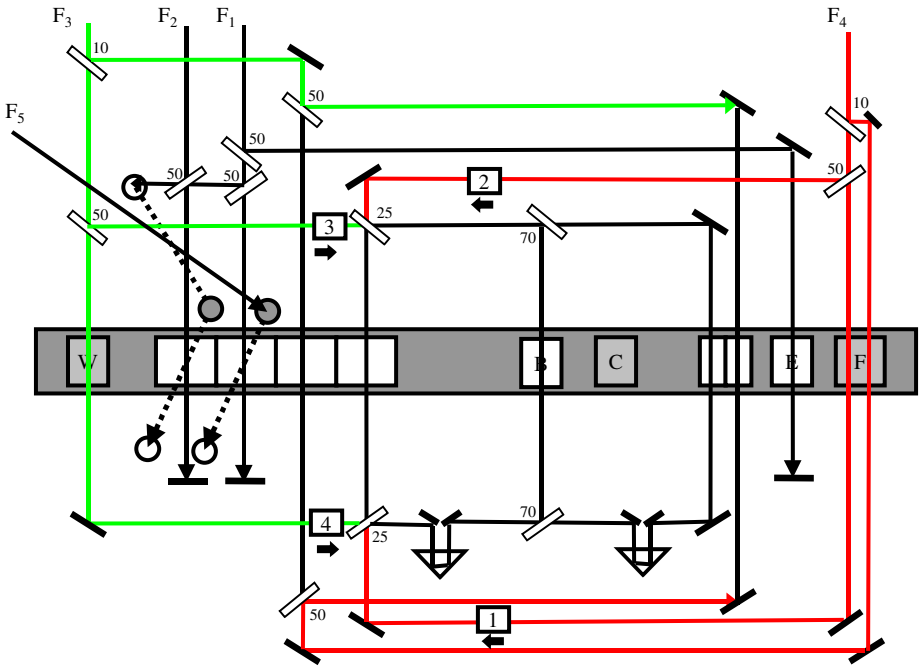

Figure 1: Bottom: Schematic illustration of the experimental setup used for demonstrating a large angle inteferometer using multi-pulse Raman excitation using ^{85}Rb atoms. Two Ti-Sapph lasers and two diode lasers, and a host of AOM's and EOM's are used to generate the various frequencies necessary in this experiment. Top: correspondence of the five required frequencies to the energy levels of ^{85}Rb.

Figure 2 shows the two-photon dark resonance, characterized by the narrow, central dip imposed on the broader single frequency spectrum, observed in the fluorescence detected as a function of the two-photon detuning. For this data, the frequencies F_2 and F_3 were nearly resonant with two optical transitions (see fig 1: top), while the difference between these frequencies was scanned by tuning the VCO driving the EOM (see section 2). The observed linewidth of the Raman dip is about 1 MHz, which is mostly due to power broadening. The fact that the dip goes almost to the bottom indicates near perfect spin-coherence excitation via the two photon process. We use this optically on-resonance dark state signal as a means to optimize the alignment of the beams to be used for the interferometer.

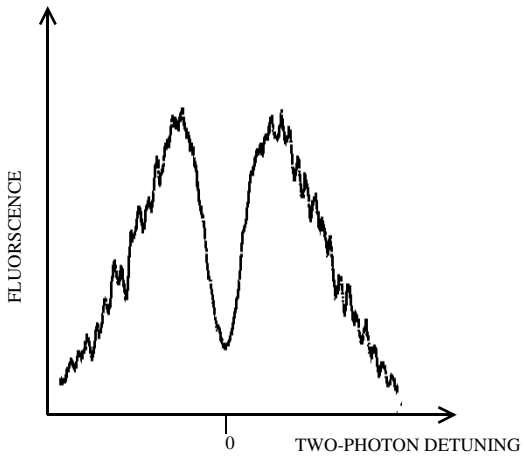

Figure 2: Observation of the Raman dip in a single zone, under co-propagating, optically resonant excitation. The central dip is power-broadened to about 1 MHz.

Figure 3 shows single zone Raman transitions, in the presence of an external magnetic field, under conditions when the frequencies F_2 and F_3 are detuned by more than 500 MHz from the excited state (see figure 1: top). The five separate lines corresponds to the five allowed Raman transitions, for our use of polarizations, among the various Zeeman sublevels. In order to observe this signal, the atoms were first optically pumped into the F=3 hyperfine level. The two-photon resonant Raman transition then transfers these atoms coherently (in a manner equivalent to microwave induced Rabi-flopping) from one Zeeman sublevel in F=3 to a corresponding Zeeman sublevel in F=2. The signal shown corresponds to the population in the F=2 level after a chosen pulse area ($< \pi$) of the interaction, monitored by detecting the fluorescence generated by exciting a cycling transition from F=2 to F'=1. As the two=photon difference frequency is tuned, the Raman excitation transfers atoms selectively from the various Zeeman sublevels, which are non-degenerate because of the applied magnetic field. The linewidth of each of these resonances is about 160 kHz, which is close to the transit time limit for a mean atomic velocity of 300 m/sec, and an optical beam width of about 2 mm.

In our interferometer, only the central one of these five transitions (which corresponds to an $F=3,m_F=0$ to $F=2,m_F=0$ transition) is to be employed, because of its relative insensitivity to magnetic fields. As such, in order to maximize the signal-to-noise ratio in our interferometer, it is necessary to transfer as much of the Zeeman sublevel populations as possible into the $F=3,m_F=0$ state prior to the Raman excitations. We have achieved this objective by using an optical pumping process where one beam, π-polarized, excites the F=3 to F'=3 transition, while another beam excites the F=2 to F'=3 transition. This sublevel state preparation is evident in figure 4, which, when compared to figure 3, shows that most of the population is now in $F=3,m_F=0$ state.

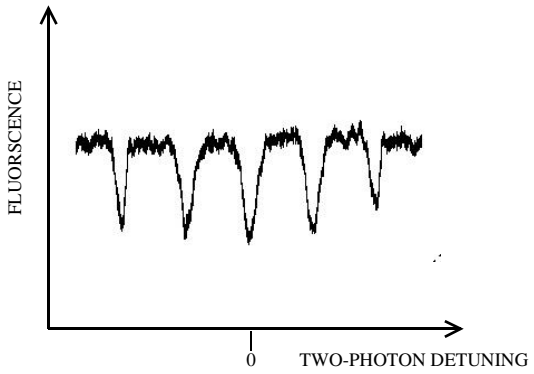

Figure 3: Observation of the five allowed Raman transitions among the Zeeman sublevels, using circularly polarized, off-resonant optical beams. One of the hyperfine levels were initially depleted via optical pumping. Fluorescence from the population pumped coherently into this level is used to monitor these resonances.

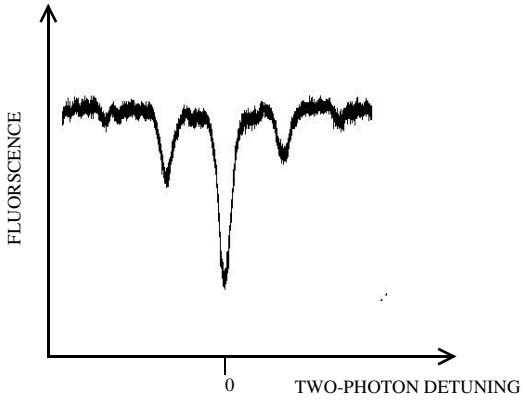

Figure 3: Two independent lasers beams, applied along orthogonal directions with properly chosen polarization, are used to increase the population of the magnetic-field insensitive Raman-transition (the central resonance), as can be seen by comparing this data with that of figure 2.

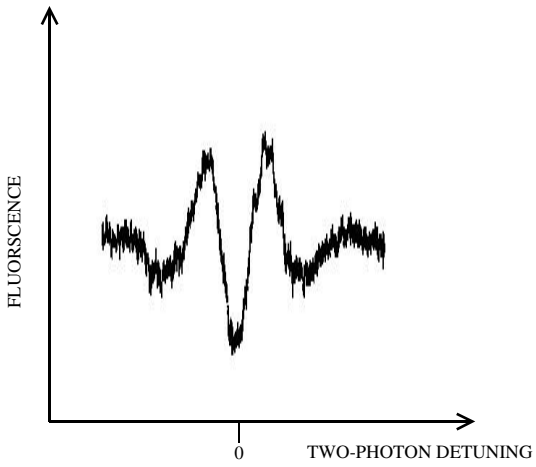

Figure 4: Observation of transit-time limited Raman-Ramsey fringes, for the magnetic-field insensitive component of the off-resonant Raman transition. The zone separation is 30 cm, and the mean atomic velocity is ~300 m/sec, so that the expected transit time width is about 1 kHz. The observed linewidth here is about 1.2 kHz, where the additional width is attributable to the velocity averaging. This (and all the signals in this section) were obtained with the injection-locked diode laser and the corresponding frequency shifted beam from one of the Ti-Sapphire (master) laser, as discussed in the section above.

In order to test the stability of our Raman transitions, we then extended the experiment to Ramsey's scheme of separated fields excitation. The resulting Raman-Ramsey fringes (corresponding to an expanded view of the central resonance in figure 3) are shown in figure 4. The damping rate of the fringes, caused by the longitudinal velocity spread, is in agreement with the theoretical velocity distribution. The zone separation is 30 cm, and the mean atomic velocity is ~300 m/sec, so that the expected transit time width is about 1 kHz. The observed linewidth here is about 1.2 kHz, where the additional width is attributable to the velocity averaging. Thus, we can conclude that the relative frequency noise between F_2 (diode laser) and F_3 (Ti-Sapphire laser) is less than 100 Hz.

We have also observed (not shown) the single zone, optically off-resonant Raman resonance for the counterpropagating case, which is the geometry to be employed for the interferometer. As is well known, this process is Doppler-sensitive, so that the linewidth is about 5 MHz, corresponding to the transverse velocity spread. While it is possible to realize the interferometer even with this velocity spread, it is desirable to reduce this spread, via cooling, in order to increase the signal-to-noise ratio. We have also observed preliminary cooling, mediated by F_1 and F_4, reducing the transverse velocity spread by about a factor of 2. Further optimization of the cooling process is currently in progress. We will attempt to demonstrate the interferometer as soon as the cooling process is optimized.

Finally, we report on a new approach we have developed for producing a two-dimensional structures with arbitrary patterns, as illustrated in figure 5. Briefly, The desired pattern (such as gears, turbines, cantilevers, etc.) is first drawn in a CAD program. The drawing is sampled as a two-dimensional function, f(x,y), from which one computes a new function: $g(x,y)=\mathrm{Cos}^{-1}(f(x,y))$. A optical intensity mask is then produced, corresponding to g(x,y). Consider next the atomic wave. The atoms dropped from the magnetic trap is first split, using a Raman resonant pulse, into two internal states. Both internal states are then defocused using a far-red-detuned laser beam with an anti-gaussian profile; this beam is pulsed on for a short time, then turned off. The expanding atomic waves are then collimated using another laser pulse with a gaussian profile. A third pulse,

on resonance, carrying the planarized intensity pattern, then interacts with only one internal state of the atoms. For a short interaction time, the laser intensity pattern acts as a linear phase mask for the atomic wave. Both internal states are then defocused and recollimated. At this point, another Raman resonant pulse is used to convert all the atoms into the same internal state, so that they can interfere. The interference pattern is Cos(g(x,y)), which yields the original pattern, f(x,y). However, this pattern is now on a scale much shorter than the optical wavelengths. For parameters that are easily accessible, in the case of rubidium atoms, it should be possible to produce patterns with feature sizes of as small as 10 nm. These patterns can be transferred to semi-conductors or coinage metals using chemical substitution techniques. Several layers can be bonded together to yield three dimensional structures, as is often done in current MEMS processes.

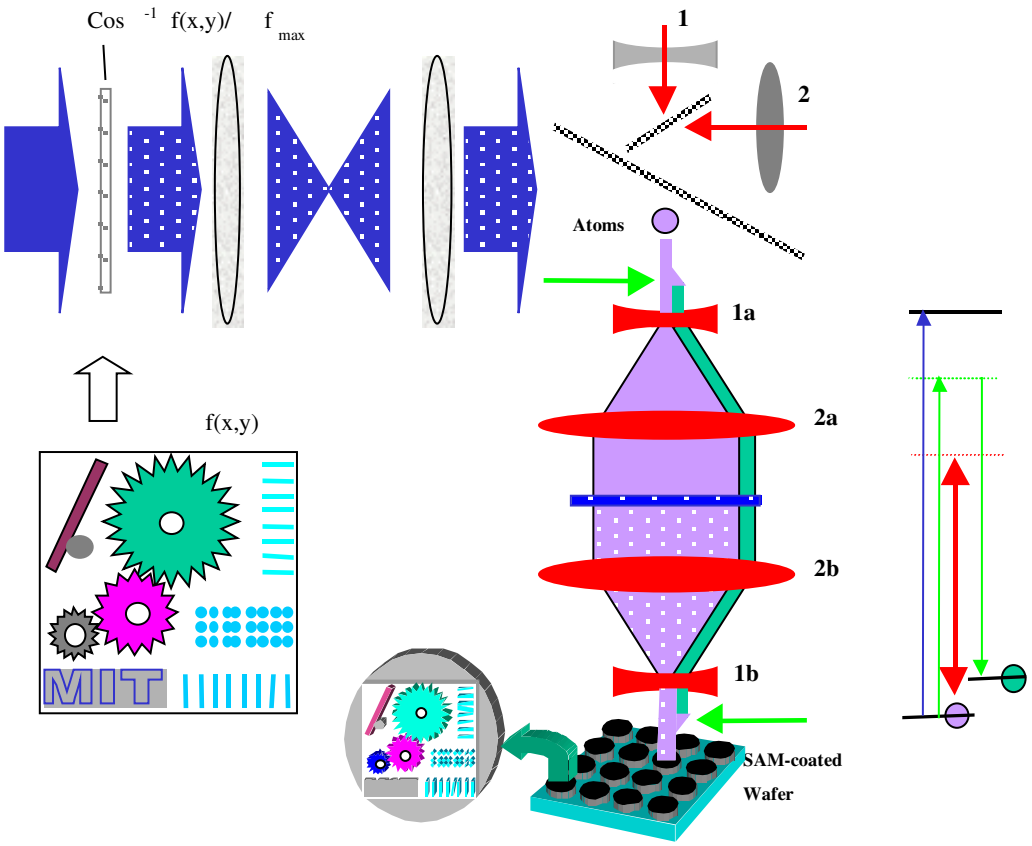

4. Experimental Demonstration of Wavelength Division Multiplexing using Polymer-based Thick Holograms

As reported previously, we have developed a novel material which is ideal for making very thick holograms with high dynamic range. Aside from applications to tera-byte scale memories, thick holograms can also be useful for making very narrow filters. Using this material, we can write as many as 20 holograms in a single substrate, each with a reflection efficiency better than 90%. With a sample thickness of 5 cm, the spectral selectivity (at any wavelength of operation) is about 3 GHz. The channels can be separated by any desired spectral distance (exceeding 3 GHz). Such a filter can be used as a multiplexer/demultiplexer in a Super Dense WDM fiber-optic communication system. The basic idea is illustrated in figure 1.

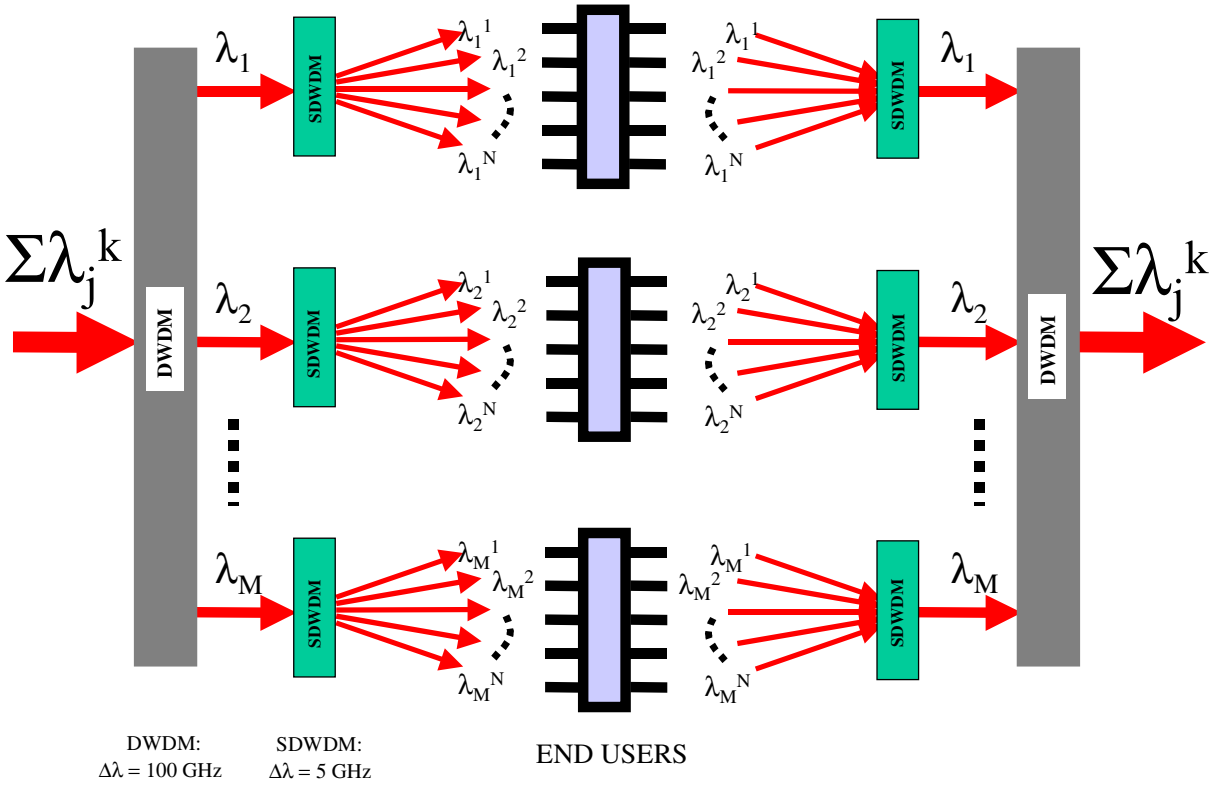

Figure 1: Schematic Illustration of the use of the Holographic Super Dense WDM (SDWDM) elements to enhance the pability of the Dense WDM (DWDM) system of fiber optic communication.

One application of this approach is in the area of optical packet switching. Consider, for example, the data traveling in one of the DWDM channels, centered around λ_j. The data would consist of several packets, each to be delivered to a different address. The individual packets could be encoded with a header stream of bits, which would contain information about the packet to follow, including its size and address. In order to switch these packets to its destination, one has to decode the header file electronically. Alternatively, one could attempt to decode the header optically and route the signal directly, using a nonlinear mixing process. For example, photon echo memory via spectral holeburning has been used to demonstrate such a process.

Using the holographic SDWDM elements as depicted in figure 1, it is possible to achieve the required switching in a simple and transparent manner. Briefly, during the encoding process, the center frequency of the modulator will be shifted to one of the sub-channels centered around λ_j^k for a packet designated for the k-th recipient. The holographic SDWDM demultiplexer will then split the packets automatically according to their distinct colors. What makes this protocol plausible is the ultranarrow bandwidth of our holograms (due to its unusual thickness), and the fact that a large number of efficient holograms can be superimposed in a single unit.

Here, we report our experimental demonstration of such a mutiplexer/demultiplexer. Briefly, three holograms were written, using green light at 514 nm from an Argon laser, in a substrate with a thickness of 1 mm, and a diameter of about 5 cm. The writing geometry was chosen carefully to ensure that these three holograms would be able to demultiplex three lasers, each operating around 676 nm, but separated in frequency by about 30 GHz (A thicker sample, which we can readily make, will enable demultiplexing of lasers much closer in frequency, as mentioned above).

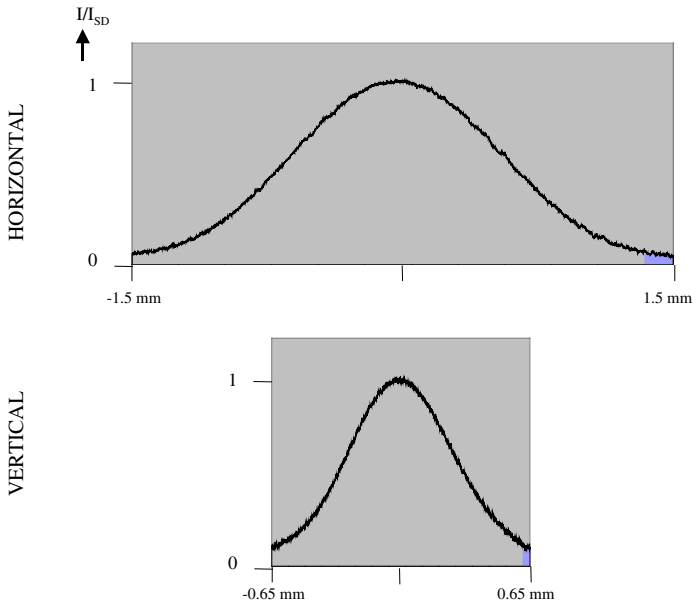

Figure 2: Experimentally measured spatial profiles of the input beam, produced by combining three independent diode lasers and two beam-splitters. The intensity, plotted in the vertical direction, is normalized to unity.

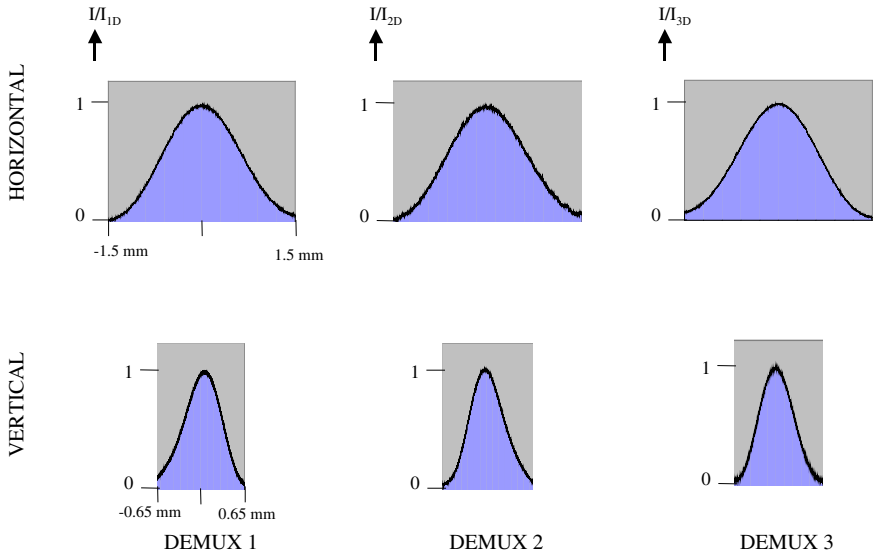

Figure 3: Experimentally measured spatial profiles of the three demultiplexed output beams, each normalized to unit intensity. The intensity, plotted in the vertical direction, is normalized to unity for each output.

In order to demonstrate the demultiplexing operation, we first combined the outputs from three independent diode lasers into a single aperture, via use of two beam splitters. The laser input intensities were chosen so that the intensity corresponding to each laser was nearly equal in the combined beam. The horizontal and vertical profiles of this beam are shown in figure 2. This was then passed through the demultiplexer. The frequencies of each laser was tuned each with a separate temperature controller, and monitored with a wave meter. As shown in figure 2, we observed three spatially separated beams, each corresponding to one of the diode lasers, with no noticeable cross-talk. The diffraction efficiency of each beam was about 88%, after taking into account fresnel reflection losses (which can be eliminated by AR coating) from each surface. Our next task is to demonstrate the demultiplexing in a sample that is 5 cm thick, with twenty different output channels.

5. Theoretical Studies and Experimental Progress Towards Quantum Teleportation of a Massive Particle for Secure Communication and Quantum Clock Synchronization:

A network of quantum computers communicating with each other reliably over macroscopic distances would be able to perform both quantum and classical computations in a secure fashion [1]. Here, we report our work toward designing and implementing a robust scheme for constructing such a quantum internet. First, we present the model we have developed for creating entanglement between two distant atoms using entangled photons. Second, we report on preliminary experimental progress towards realizing this goal with trapped rubidium atoms.

Any two atoms that share entanglement can exchange quantum information by the process of teleportation [2]. Even if two atoms do not share entanglement, they can still exchange quantum information through a series of links that do share entanglement. Quantum information

processing need only be performed locally, within the nodes. The scheme should allow the reliable transmission of quantum information between quantum microcomputers separated by distances of hundreds of kilometers.

In general, it is difficult to create a quantum wire, i.e., a quantum communications channel that can transmit quantum information [3]. Direct quantum communication is fragile; although methods exist for coping with noisy quantum channels, they are complicated and require considerable computational time [4]. The solution is to create a quantum internet that does not require reliable quantum wires [5]. Cavity quantum electrodynamics provides mechanisms for communicating between cavities using inter-cavity photons [1,5]. The key technology proposed here is a method for transmitting quantum entanglement over long distances, capturing it in optical cavities, and storing it in atoms.

We describe the method in general terms and provide specific details later. First, use parametric down conversion to create pairs of photons that are entangled both in momentum and in polarization. Send one photon to cavity 1 and the other to cavity 2, equidistant from the source. Each cavity contains an ultra-cold atom, trapped in an optical lattice in vacuum. Because of their momentum entanglement, each of the entangled pair of photons arrives at its respective cavity at the same time. Although many (indeed most) of the photon pairs will fail to arrive and enter their respective cavities, on occasion a photon will enter cavity 1 and its entangled pair photon will enter cavity 2 at the same time. Once in the cavity, the photon can drive a transition between the A and the degenerate B levels of the atom (see figure 1a). This effectively transfers the photon entanglement to the degenerate B levels of the atoms in cavities 1 and 2.

This entanglement can be detected and stored as follows. Concentrate first on a single cavity. To protect the quantum information in the event that the atom has absorbed the photon, drive a coherent transition from the degenerate B levels to the long-lived D hyperfine levels as in figure 1a. Now detect whether or not the atom has absorbed a photon by driving a cycling transition from the A to the C level of the atom. If no fluorescence is seen, then the atom successfully absorbed the photon and the resulting entanglement in D will be stored for subsequent manipulations. On the other hand, if fluorescence is observed, then the atom was still in A, which means it failed to absorb the photon. In this case the atom will be allowed to return to A (from C), ready to absorb the next photon that enters the cavity. When the keeper of cavity 1 has successfully captured a photon, she notes the time of arrival and calls the keeper of cavity 2 over the phone to see whether he has successfully captured a photon at the same time. If not, she returns her atom to the state A and tries again. If both cavity keepers have captured a photon at the same time, however, they now possess two distantly separated atoms that are entangled.

The above method allows the creation of entanglement between atoms separated by long distances in the face of arbitrarily high loss rates, in principle. In practice, the fidelity of the entanglement created is determined by the accuracy with which one is able to perform the various operations used to capture and store entanglement. First, account for the losses with probability λ that a photon survives its long trek from source to cavity and is absorbed by an atom. We can write $\lambda = 10^{-L/10}$, where L is the net loss in decibels. If λ is small, then most of the time the atom will be in A, and the fluorescence will be observed on the cycling transition. Occasionally however, the detector will fail to detect this fluorescence and erroneously conclude that the atom is in D, when in fact it is not. The false detection probability can be written as $\varepsilon = p^N$ where p is the probability that the detector fails to detect a single photon and N is the total number of cycles that the cycling transition is repeated. Alternatively, the false-positive probability can be expressed in terms of the (effective) signal-to-noise ratio of the cycling transition S as $\varepsilon = 10^{-S/10}$. The fidelity is high as long as $\varepsilon << \lambda$, which means that when the cavity keepers believe that they have both successfully captured photons, they are almost always right. Clearly the fidelity can be increased to the desired level by driving the cycling transition longer. Of course, this is limited by the probability of driving an off-resonant transition to a non-cycling state. Fortunately, in practice not many cycles are needed. The main problem with high losses is that

the entanglement capture procedure must be repeated ~$1/\lambda^2 = 10^{L/5}$ times in order to capture a single entangled pair. This will be discussed in more detail below.

Fidelity can also be degraded by spontaneous emission from the excited state, but this can be minimized by using off resonance Raman excitation. To improve entanglement fidelity further, many atoms can be included in the trap and entanglement purification techniques can be used [6]. Finally, to store and maintain the entanglement for times long compared with the decoherence time of the atoms, one can in principle combine entanglement purification together with the use of quantum error correcting codes [7]. However, because of the long coherence time of atoms in the proposed method this should not be needed.

Let us now look at how such a scheme might be carried out in practice using rubidium atoms (figure 1b). A UV laser (pulse or CW) will be used to excite a non-linear crystal. Via type-II parametric down-conversion, this crystal will produce pairs of entangled photons, each at 795 nm. A brighter source of photon pairs is described in ref. [8]. We consider the polarization entanglement to be of the form $(|\sigma_+>_1|\sigma>_2 + |\sigma>_1|\sigma_+>_2)/\sqrt{2}$, where $\sigma_+(\sigma)$ indicates right(left) circular polarization. Each beam is coupled into a fiber, and transported to a resonant, high-finesse optical cavity with slow decay and a strong vacuum rabi frequency (20 MHz) [9].

Each cavity, at its center, holds a single rubidium atom, confined by a focused CO_2 laser. The mean number of atoms caught is controlled via the parameters (e.g., the initial trap depth) involved in the process. Starting with a mean-value of about 5, the atoms will be knocked out one by one (e.g., via photo-ionization), while monitoring the remaining fluorescence until only a single atom remains. It has been demonstrated recently [10] that at a pressure of 10^{-11} Torr, atoms survive for more than 2 minutes in a CO_2 trap. The trap lifetime, and hence the decoherence time, can be increased up to an hour by housing the trap chamber in a liquid helium cryostat.

To load the photon into the cavity, one approach, akin to ref. 1, is to use a carefully timed and shaped Raman pulse to induce the simultaneous admission of the photon into the cavity and absorption by the atom. In the more general case, when the temporal envelope of the photon cannot be controlled, the cavity will still load with some probability η which can be enhanced by proper choice of cavity and laser pulse (B-D transition) parameters. It is important to note that due to the momentum entanglement the probability of absorbing two conjugate photons is also η not η^2.

Figure 2 illustrates the energy levels and transitions to be employed. Initially, the atom(s) are prepared to be in the F=1, m_F=0 ground state (`A' level). The photon excites the dashed transitions to the F=1, $m_F=\pm1$ excited level (`B' levels) (fig 2a). A π polarized beam completes the Raman excitation, putting the atom in a superposition of the F=2, $m_F=\pm1$ ground states ('D' levels). To detect whether the photon has been absorbed by the atom, the F=1 ground state is detected by exciting the cycling transition ('A to C') shown in figure 2b using a 780 nm beam. The same process occurs at the other cavity, and the results sent to a co-incidence monitor, as shown in figure 1b.

Let us now insert reasonable numbers for losses and errors and see how far this method is likely to operate without the use of quantum repeaters [11]. Realistic optical fiber losses for 795 nm photons are 3dB per kilometer. Putting the two cavities 10 kilometers apart gives a per-cavity loss rate of *L* ~ 15 dB, assuming that losses are dominated by the fiber. Sensitive photodetectors along with appropriate optics can give a photon detection rate of 25%. Hence, driving the cycling transition 30 times gives a signal to noise of ~ 37 dB, more than adequate to compensate for fiber loss. The entanglement creation rate can be estimated by multiplying the fluorescent photon emission time (30 nanoseconds) by the number of cycles and the mean number of times the capture procedure must be repeated ($10^{2L/10}$) to yield one pair per millisecond. Accordingly, a distance of ten kilometers between nodes of the quantum internet seems a reasonable objective.

The two cavities now contain atoms that are entangled with respect to long-lived states. This entanglement can be used for quantum teleportation, quantum cryptography, superdense coding, or what you will. Here, we show an explicit construction for performing the teleportation of a quantum state, as illustrated in figure 3. Briefly, the entangled atoms are atom 2 (with Alice) and atom 3 (with Bob). Alice now has a third atom (atom 1), whose quantum state she will teleport. Atom 1 is trapped in another node of the CO_2 beam, and shares a second cavity with atom 2 (figure 3a). In what follows, we adopt the abbreviated state designations for the $5^2S_{1/2}$ sublevels most relevant to our discussion: $|a\rangle \equiv |F=2,m_F=-1\rangle$, $|b\rangle \equiv |F=2,m_F=+1\rangle$, $|c\rangle \equiv |F=1,m_F=-1\rangle$, and $|d\rangle \equiv |F=1,m_F=+1\rangle$.

Assume that the state of atoms 2 and 3 can be written as $|\psi_{23}\rangle = \{|a\rangle_2|b\rangle_3 + |b\rangle_2|a\rangle_3\}/\sqrt{2}$. Alice can put atom 1 into an unknown state $|\varphi_1\rangle = \{\alpha|c\rangle_1 + \beta|a\rangle_1\}$ by using an optically off-resonant (OOR) Raman pulse of unmeasured duration that couples $|c\rangle_1$ to $|a\rangle_1$. For concreteness, we rewrite $\alpha(t)=\alpha_0$ and $\beta(t)=\beta_0\theta(t)$, where $\theta(t)=\exp[-i(\omega_M t+\xi)]$, the frequency ω_M and phase ξ being determined by those of the oscillator used to generate the second Raman frequency from the first. Using the scheme of Pellizzari et al. [12], which can be realized using the transitions shown in figure 3b, Alice transfers the state of atom 1 into atom 2, leaving atom 1 in a pure state $|c\rangle_1$, and atoms 2 and 3 in the state $|\phi_{23}\rangle = \{|A_+\rangle(\alpha_0|b_3\rangle + \beta_0|a_3\rangle) + |A_-\rangle(\alpha_0|b_3\rangle - \beta_0|a_3\rangle) + |B_+\rangle(\beta_0|b_3\rangle + \alpha_0|a_3\rangle) + |B_-\rangle(-\beta_0|b_3\rangle + \alpha_0|a_3\rangle)\}/2$, where the Bell basis states are given by $|A_\pm\rangle = \{|c_2\rangle \pm \theta|b_2\rangle\}/\sqrt{2}$, and $|B_\pm\rangle = \{|d_2\rangle \pm \theta|a_2\rangle\}/\sqrt{2}$.

To measure the Bell states, Alice first applies a set of pulses that maps the Bell states to bare atomic states. Consider the states $|A_\pm\rangle$. Alice applies an OOR Raman $\pi/2$ pulse, coupling $|c_2\rangle$ to $|b_2\rangle$, using a σ_+ polarized light at ω_1 and a σ_- polarized light at ω_2, where $\omega_1 - \omega_2 = \omega_M$ (see figure 4a). The off resonant pulses are tuned near the F=1 excited state to avoid interactions between $|a_2\rangle$ and $|d\rangle_2$. She generates ω_2 from ω_1 using an oscillator with a known phase shift of ξ. She chooses $\xi = -\pi/2$, converting $|A_+\rangle$ to $|c_2\rangle$, and $|A_-\rangle$ to $|b_2\rangle$. Similarly, she applies another OOR Raman $\pi/2$ pulse with different polarizations to convert $|B_+\rangle$ to $|d_2\rangle$, and $|B_-\rangle$ to $|a_2\rangle$.

Alice can now measure the internal states by using a method of sequential elimination. First, she applies a Raman pulse to transfer the amplitude of state $|d_2\rangle$ to an auxiliary state in the $5^2S_{1/2}$, F=2 manifold (see figure 4b). A magnetic field can be applied in order to provide the necessary spectral selectivity. She then probes the amplitude of state $|c_2\rangle$ by driving the $5^2S_{1/2}$, F=1 to $5^2P_{3/2}$, F=0 cycling transition. If she detects fluorescence, she concludes that the atom is in state $|c_2\rangle$, which in turn means she has measured the Bell state $|A_+\rangle$. If she fails to see fluorescence, then she has eliminated this possibility, and now applies a Raman pulse to return the amplitude of the auxiliary state to state $|d_2\rangle$. She again drives the cycling transition, and detection of fluorescence implies she has measured the Bell state $|B_+\rangle$. Otherwise, she applies a set of Raman pulses to transfer the amplitude of $|a_2\rangle$ to $|c_2\rangle$ and $|b_2\rangle$ to $|d_2\rangle$. She now repeats the detection scheme for state $|c_2\rangle$. If she sees fluorescence, the atom is in $|c_2\rangle$, which implies that she has measured $|A_-\rangle$. If not, she has eliminated three possibilities, which means that the system is in $|B_-\rangle$.

Alice now sends a two-bit classical message to Bob, informing of which state she has found the world to be in. Bob now has to make some transformations to his atom in order to produce the state $|\phi_1\rangle$ in atom 3. This he can accomplish as follows. If Alice found $|A_+\rangle$, Bob does nothing, and atom three is already in state $|\phi_1\rangle$. On the other hand, if Alice found $|A_-\rangle$, then Bob has to flip the phase of $|a_3\rangle$ by π with respect to $|b_3\rangle$. This can be achieved by applying an OOR Raman 2π pulse connecting $|a_3\rangle$ to the auxiliary ground state $|F=1,m_F=0\rangle$ via the $|F=0,m_F=0\rangle$ state in $5^2P_{3/2}$. Atom 3 is now in state $|\phi_1\rangle$, as desired. If Alice found $|B_+\rangle$, then Bob first applies an OOR Raman π pulse coupling $|a_3\rangle$ to $|b_3\rangle$ to swap their amplitudes, again producing the desired state. Finally, if Alice found $|B_-\rangle$, then Bob first applies a π pulse as above to swap amplitudes, followed by the 2π pulse for the π phase change, producing the desired state.

Such teleportation allows the robust transfer of quantum information from cavity to cavity in principle. Since each cavity in and of itself constitutes a quantum 'microcomputer,' our design for a quantum internet is now complete: quantum information is processed at the atomic scale, passed from atom to atom within each cavity using the cavity field, and passed from cavity to cavity using teleportation.

We have also devised an explicit scheme for realizing a novel scheme for synchronizing atomic clocks via entangled states shared a priori between two clocks[13]. This process has exciting applications in very long base line interferometry (VLBI), as well as in the global positioning system (GPS). Currently, the precision of the GPS is limited by the index fluctuation of the atmosphere, since the propagation time of classical synchronizing signals fluctuate randomly. The method based on entanglement will eliminate this limitation.

In order to implement this approach, it is necessary to use atomic clocks that will use only a few, distinct atoms. The atomic clocks based on using vapors or atomic beams are inappropriate for this task. Instead, what is necessary is a system which will have a small number of single atoms, each caught in a trap. Of course, such clocks have been realized using single trapped ions. In the same manner, it is possible to realize an atomic clock using a single neutral atom caught in a dipole force trap, of the kind proposed in our MURI project. In particular, a two-photon induced excitation of the hyperfine transition in ^{87}Rb can be used to realize such a clock. This type of atomic clock, called the Raman clock, was demonstrated originally by members of our group[14]. Compared to direct RF-excited clocks, the Raman clock has a distinct advantage here. The Jozsa protocol calls for at least two clocks (i.e., two atoms) at each location. The Raman excitation can be localized to a very small volume: ~ $[10\ \mu m]^3$. As such, it can address the two clocks separately, within a small physical volume. In addition, it eliminates the need for microwave cavities altogether.

In the model we are considering, the atoms held by Bob (Alice) in the dipole force traps would be his (her) atomic clocks. In order to accommodate the need for determining a shared origin of time, it will be necessary to deal with two different of clocks at each location, each with a clock transition frequency slightly different from the other. This requirement can be met by introducing a light shift via an imbalance in the laser intensities for the Raman clock transition one of the ^{87}Rb atoms. The overall concept is illustrated schematically in figure 5.

As discussed above, in order to realize the teleportation, we will use trapped rubidium atoms. We are currently characterizing and modifying our existing rubidium trap apparatus to this end. In particular, we have measured the temperature of the trapped atoms using a time of flight method. The preliminary result is shown in figure 6. This information is now being used in designing a fountain launching system, which will send the atoms upward. FORT traps, created by a Ti-Sapphire laser tuned to 830 nm, will be used to capture a few of the cold atoms at the top of the fountain, so that the residual kinetic energy would be minimal. The high finesse optical cavities will be centered around the waist of the FORT. Cavity pulling effects will then be used to make sure only one atom remains in each FORT focus.

References:

1. J. Cirac et al., *Phys. Rev. Lett.*, **78**, p. 3221 (1997).
2. C. Bennett et al., *Phys. Rev. Lett.*, **70**, p. 1895 (1993).
3. S. Lloyd, *Science*, **261**, p. 1569 (1993).
4. C. Bennett, D.DiVincenzo, J.Smolin, *Phys. Rev. Lett.*, **78**, p. 3217 (1997); B. Schumacher and M. Nielsen, *Phys. Rev. A*, **54**, p. 2629 (1996); B. Schumacher, *Phys. Rev. A*, **54**, p. 2614 (1996); S. Lloyd, *Phys. Rev. A*, **55**, p.1613 (1997).
5. S. van Enk, J. Cirac, P. Zoller, *Phys. Rev. Lett.*, **78**, p. 4293 (1997)
6. P. Shor, *Proceedings of the 37th Annual Symposium on the Foundations of Computer*

Science, IEEE Computer Society Press, Los Alamitos, p. 56 (1996); D. DiVincenzo and P. Shor, *Phys. Rev. Lett.*, **77**, p. 3260 (1996).
7. P. Shor, *Phys. Rev. A*, **52**, pp. R2493-R2496 (1995); A. Steane, *Phys. Rev. Lett.*, **77**, pp. 793-797 (1996); A. Calderbank and P. Shor, *Phys. Rev. A*, **54**, pp. 1098-1106 (1996); R. Laflamme, C. Miquel, J. Paz, W. Zurek, *Phys. Rev. Lett.*, **77**, p. 198(1996); E. Knill and R. Laflamme, *Phys. Rev. A*, **55**, p. 900 (1997); C. Bennett et. al., *Phys. Rev. A*, **54**, p. 3824 (1996).
8. J. Shapiro and N.Wong, submitted to *Opt. Letts*.
9. S. Morin, C. Yu, and T. Mossberg , *Phys. Rev. Lett.* **73**, p.1489 (1994).
10. K. O'Hara et. al., *Phys. Rev. Lett.* **82**, p. 4204 (1999).
11. H. Briegel et. al., *Phys. Rev. Lett.,* **81**, p. 5932 (1998).
12. T. Pellizzari et. al., *Phys. Rev. Lett.*, **75**, p. 3788 (1995).
13. R. Jozsa, D.S. Abrams, J.P. Dowling, and C.P. Williams, quant-ph/0004105
14. M.S. Shahriar and P. R. Hemmer, *Phys. Rev. Lett.*, 65, 1865(1990)

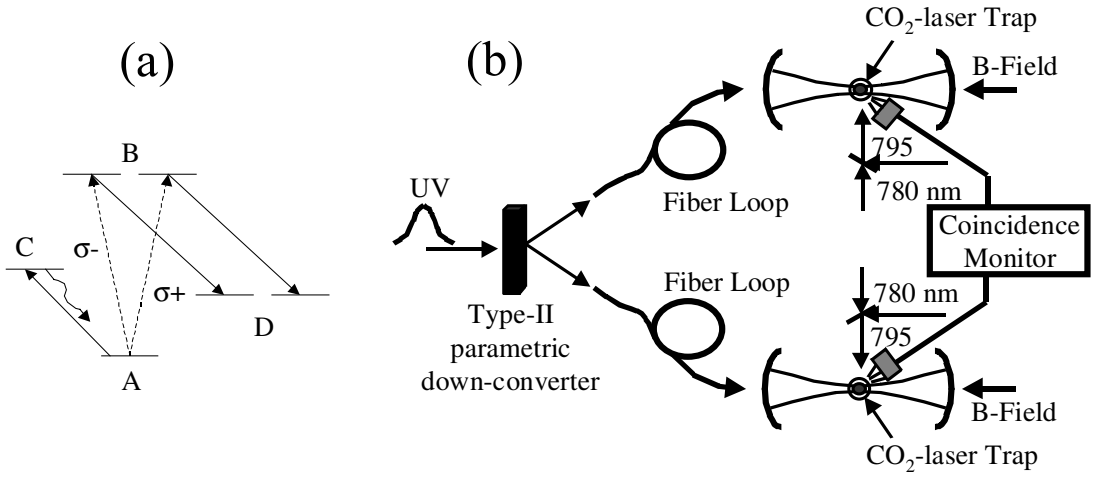

Figure 1. Schematic illustration of the proposed experiment for creating potentially long distance entanglement between a pair of trapped rubidium atoms (see text)

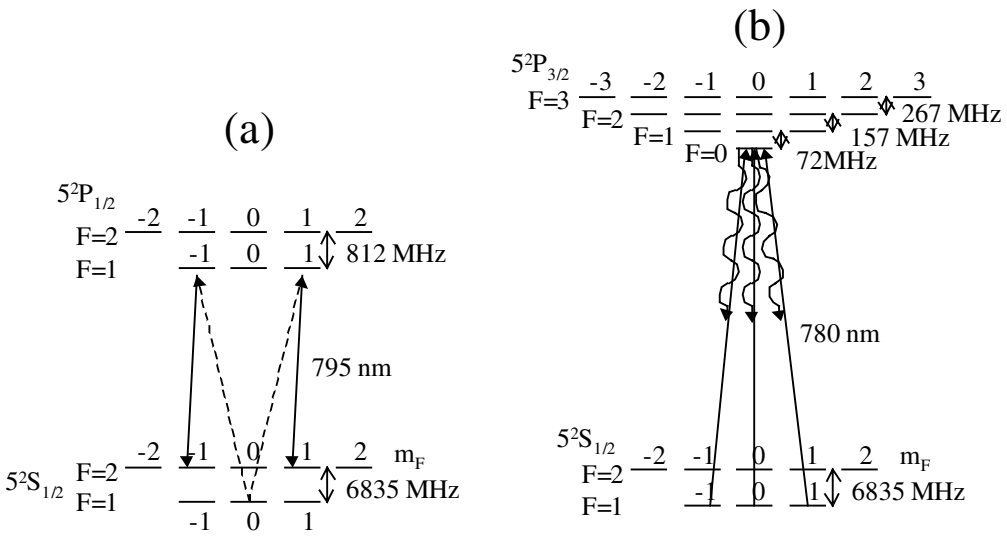

Figure 2. Schematic illustration of the steps to be used in storing quantum coherence in a rubidium atom, and detecting it non-destructively (see text).

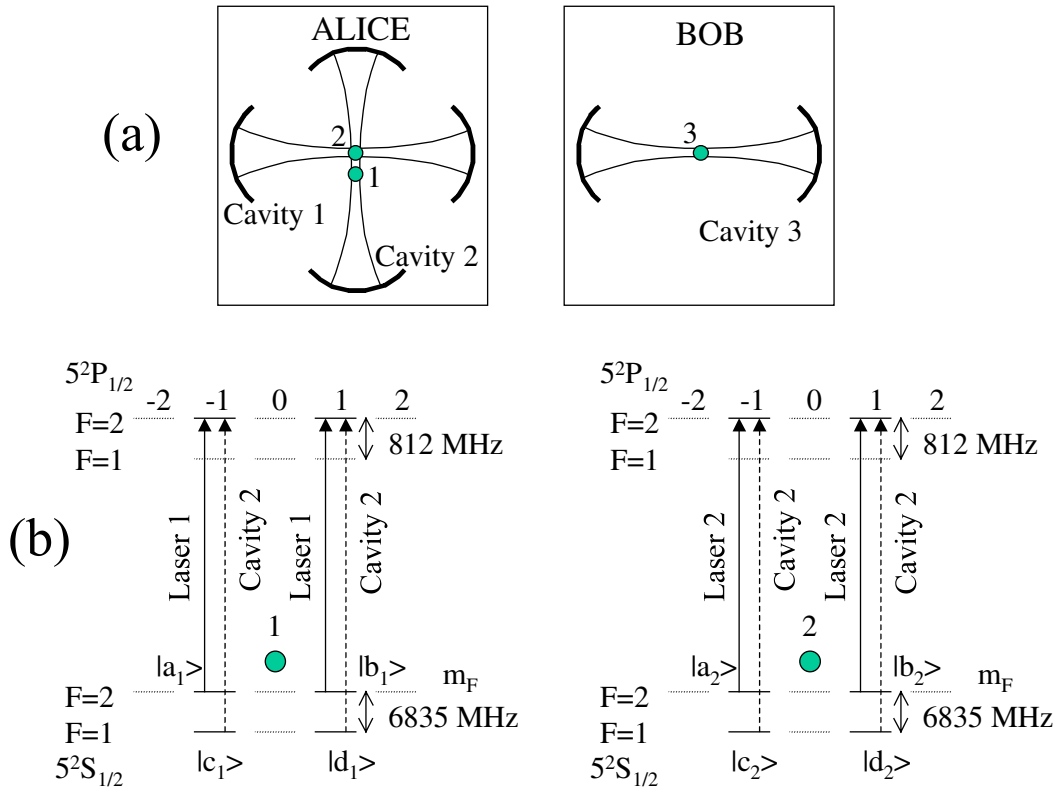

Figure 3: Teleportation using trapped Rb atoms: (a) Atom 2 (with Alice) and atom 3 (with Bob) are entangled via storage of the entangled photon pairs, as described above. Atom 1 (also with Alice) is held by a second CO_2 laser node, and shares a common cavity that is orthogonal to the one used for capturing the entangled photons. (b) Basic model for Alice to transfer the coherence from atom 1 to atom 2, in preparation for teleportation.

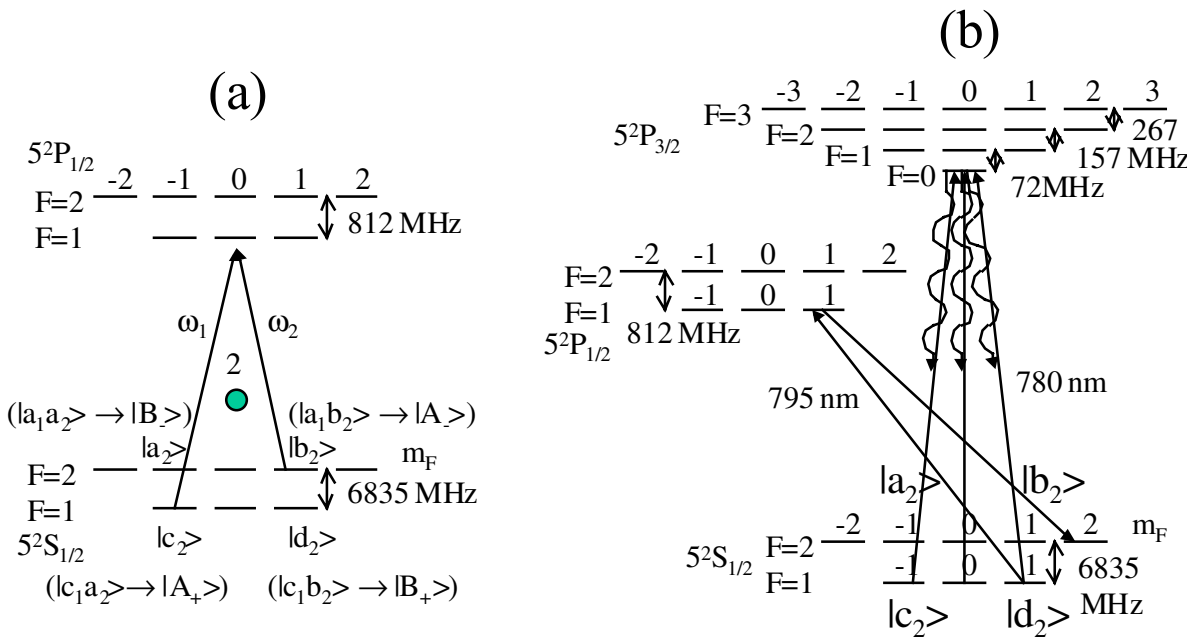

Figure 4. Bell state measurement: (a) Off resonant Raman transition used to map the amplitudes of the Bell states onto the bare atomic states (b) Bell state detection is done sequentially using Raman transitions (see text).

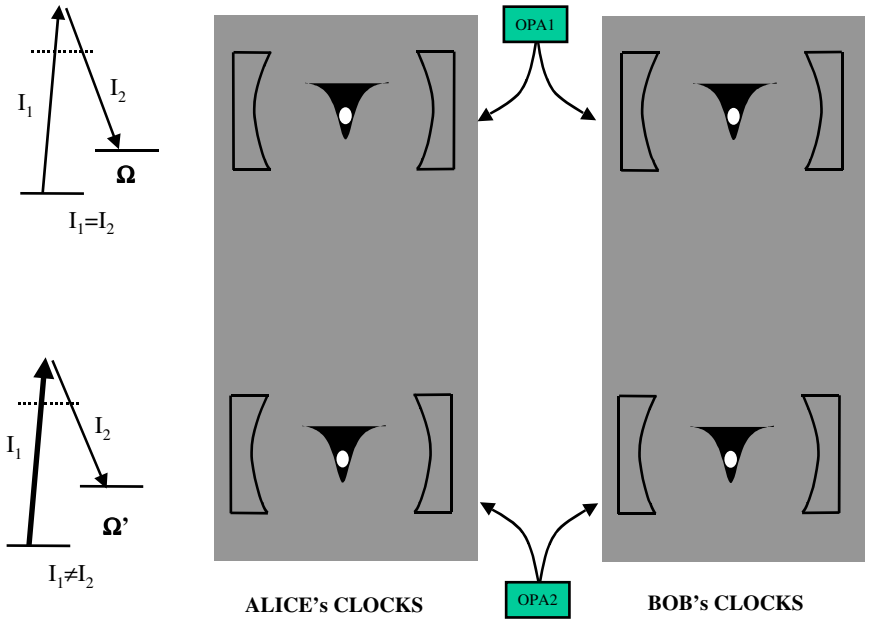

Figure 5: Illustration of the configuration to be considered for synchronizing Raman atomic clocks using shared entanglement between atom pairs, produce via storing entangled photon pairs from OPA's. The off-resonant two-photon transitions depicted on the left are equivalent to direct RF transitions, and hence can be used to realize localized single atom clocks, without requiring RF cavities. The use of unbalanced laser intensities on one of the clocks lifts the degeneracy by introducing a light shift, as needed for determining absolute time references.

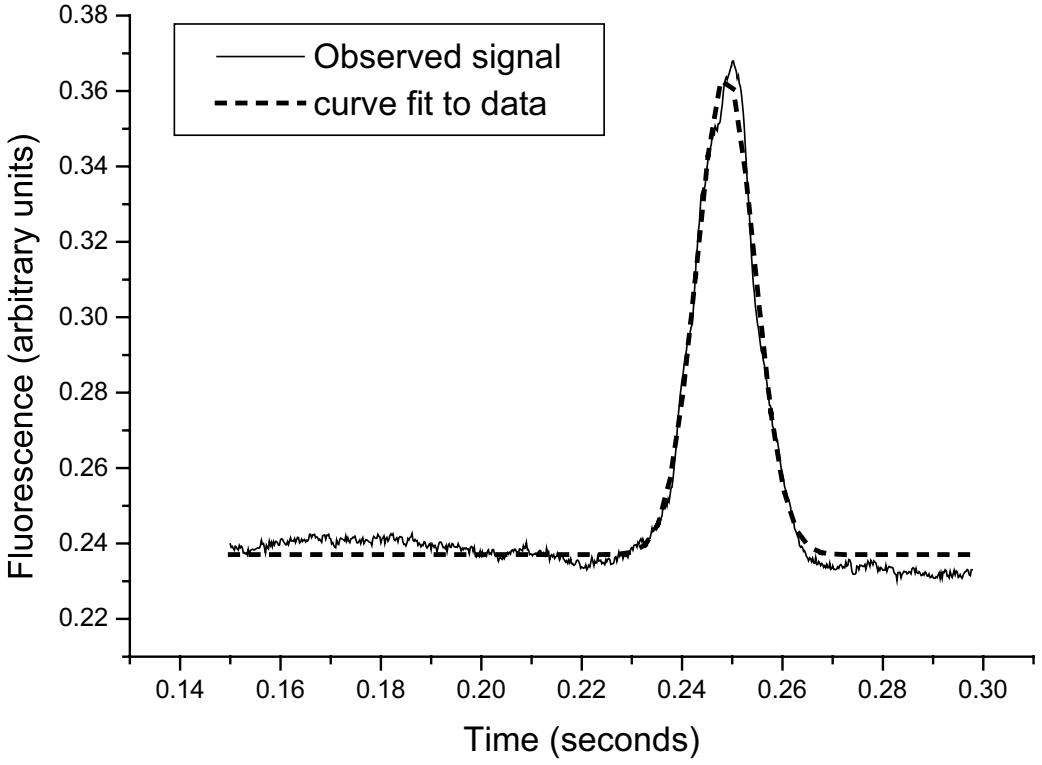

Figure 6: Experimental data, with corresponding theoretical fit, for measuring the temperature of the atoms in our trap. The trapped atoms were dropped from the center, and the arrival time was recorded by monitoring fluorescence from a sheet of light located about 30 cm below the trap. From the geometry and the timing information, we determine that the temperature of our trapped sample is 14 μK. Further cooling is possible, but may not be necessary for our scheme, where only a few cold atoms have to be caught using FORT beams.

6. Technical Progress Towards Automatic Target Recognition and Content-based Data Mining using Polymer-based Thick Holograms

Previously, we have reported storage and recall of many pages of data in a holographic sample made in our group, using a material called PDA. Currently, we are constructing a unit that will demonstrate rapid identification of a stored image via optical correlation. Briefly, we will store in an MMU (multiplexed memory unit) about a million (1,024,000, to be exact) images of various objects, viewed from different distances and perspectives. For our purposes, many copies of the same image would be used. We will then demonstrate that any one of these images can be identified via optical correlation with the stored images in the MMU. Here, we report the technical progress we have made towards this goal.

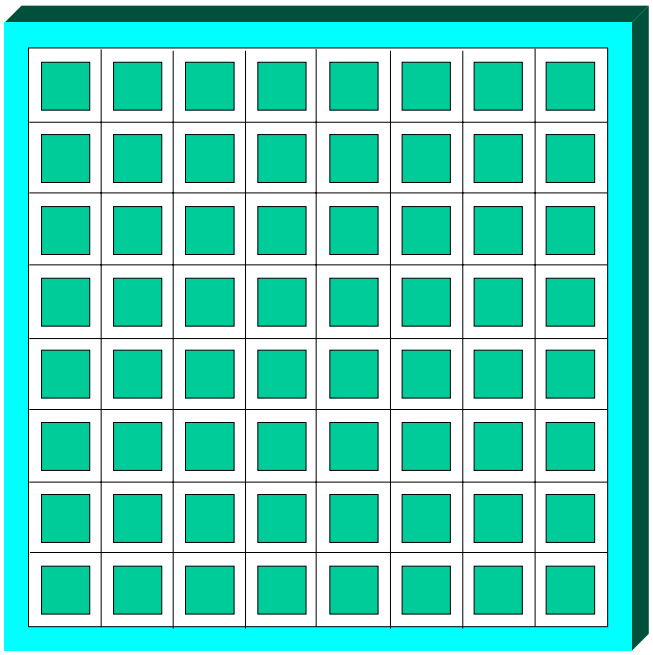

Figure 1: Schematic illustration of the MMU (multiplexed memory unit), with a dimension of 124mm X 124mm X 2mm. The number of sub-units is 1600, although only 64 are shown for clarity. Each sub-unit has a dimension of 2mm X 2mm, and separated from one another by a 1 mm wide guard strip in all directions.

The MMU is shown schematically in figure 1. We have made many copies of such a sample, with a square dimension of 124 mm X 124 mm, and 2 mm wide guard strip on each side. The active area of 120 mm X 120 mm is sub-divided into smaller squares, each 3 mm X 3 mm,. This corresponds to a total of 1600 sub-divisions. The sub-divisions are separated from one another by a 1 mm guard band on each side. This is necessary in order to allow the angular multiplexing.

The sample has a thickness of 2 mm, corresponding to an angular selectivity of about 0.25 mrad, for a writing wavelength of 514.5 nm. We use an angular separation of 0.5 mrad between each data page. Each subdivision stores 640 pages, corresponding to an angular spread of ±9 degrees. The reference beam is at an angle of 30^{o} with respect to the normal to the sample. The image beams, corresponding to the 640 data pages, spans the range of -21^{o} to -39^{o}. This is illustrated in figure 2.

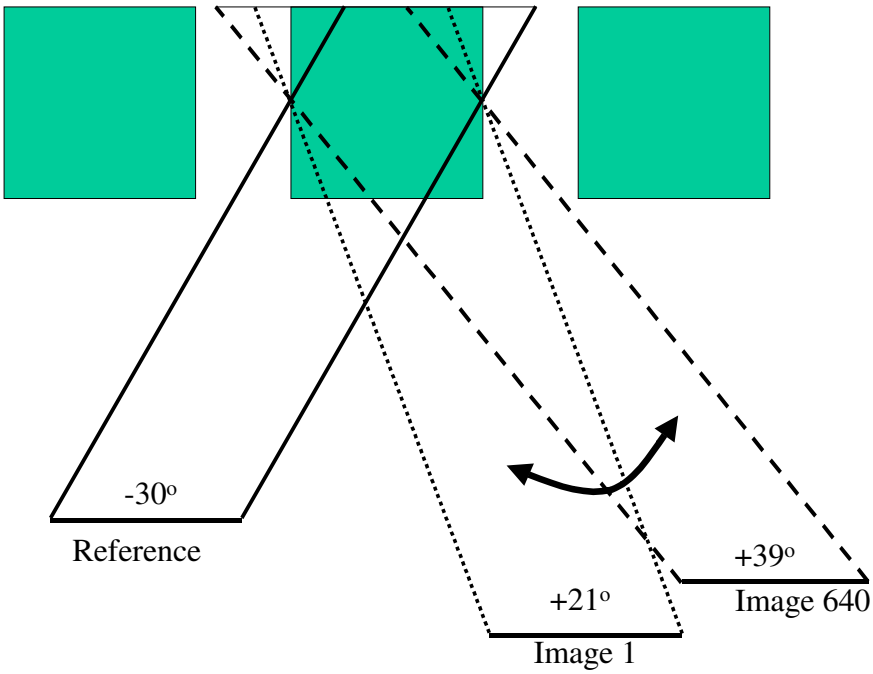

Figure 2: Schematic illustration of the angular multiplexing geometry, drawn to scale. The reference and image beams are incident on the MMU from the front. The reference beam is held fixed at –30°, while the image beam is scanned from +21° to +39°, in increments of 0.5 mrad. Note that the 1 mm wide guard band is wide enough to eliminate potential cross-talks between neighboring sub-units.

In order to write the data at each of the subdivisions, we have devised a two-dimensional scanning system, shown schematically in figure 4. The assembly consists of two different positioners. The MMU is secured to the fine positioner (FP), and the FP is secured to a coarse positioner (CP). Assume first that the CP has moved the sample to within 0.5 mm in both X and Y directions. The FP is then used to position the MMU precisely. This accomplished by using a feedback system. A diode laser is mounted at a position that remains fixed with respect to the writing apparatus. A screen, fastened to the FP, and parallel to the MMU, moves around in front of the diode laser as the FP moves the MMU. The surface of this screen (e.g. metal coated plastic) reflects the light back, which in turn is redirected to a photo-detector. This surface has a number of holes, equaling the number of MMU sub-units, and separated from each other by the same distance as the MMU sub-units. The hole diameter is about 0.5 mm, while the laser beam diameter is about 1 mm. As such, the laser beam is aligned perfectly with the hole when the detector signal is minimized. A simple servo is used to guide the FP, first in he X direction, and then in the Y direction until this position is reached. Note that the MMU and the reference screen are mounted on a single bar, which in turn is connected to the FP. After the data has been stored, the MMU and the reference screen has to stay fastened to this bar at all times; otherwise, a painstaking (but not impossible) procedure has to followed to re-establish the one to one correspondence between the MMU sub-units and the holes in the reference screen.

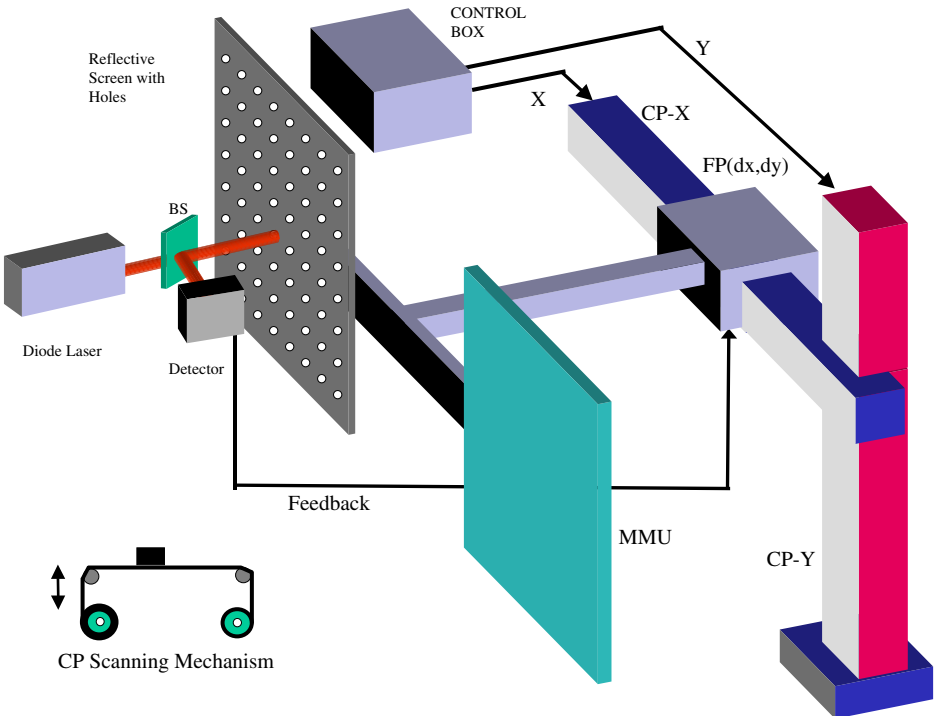

Figure 3. Schematic Illustration of the 2D scanning mechanism.

In order to demonstrate the automatic target recognition, we have developed a data base containing pictures of actual military targets, including planes, tanks, armored vehicles and missiles. Altogether, we have put together a library of 2560 (=4X640) images. Each image has been converted to a reduced image represented by 256X256 bits. This step is identical to what we had done in converting frames from a skating video during our earlier demonstration of holographic image storage and read-out. Figure 4 shows a sample of these 8 kbyte images for a particular plane, pictured from different distances an orientations. These images are called the raw image files (RIF's). The RIF's have been named sequentially for automatic access, and stored in a hard drive. These 2560 images are repeated 400 times to fill out the 1600 memory sub-units. The writing set up is illustrated in figure 5. Briefly, an Argon laser is used as the source. The laser beam is split into two parts, one for the reference and the other for the object. The object beam reflects off the SLM, which has the image file downloaded from the computer. The reference beam is scanned using two mirrors so that angular multiplexing is possible without spatial shifting. A timing system makes sure that the whole operation proceeds synchronously.

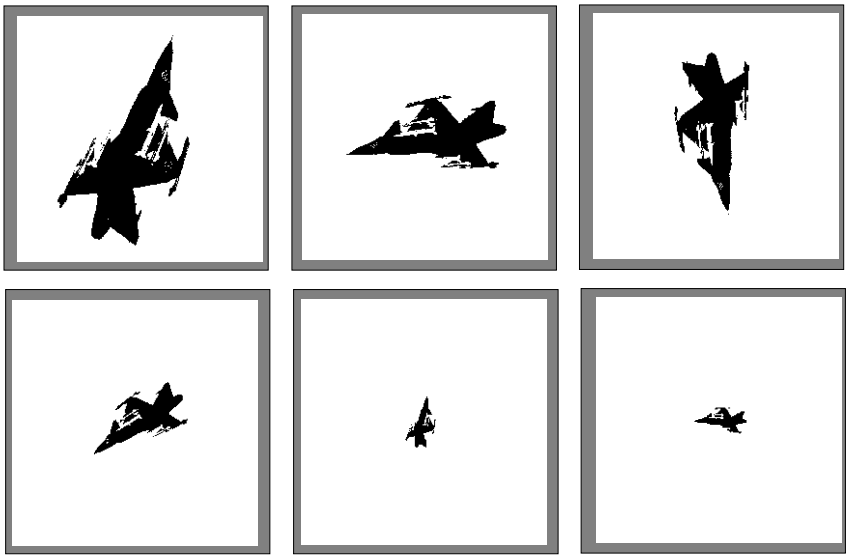

Figure 4: Different sizes and orientations of the same plane, recorded in a 256X256 bit grid. The correlator would be able to distinguish not only between different planes, but different orientations of the same plane.

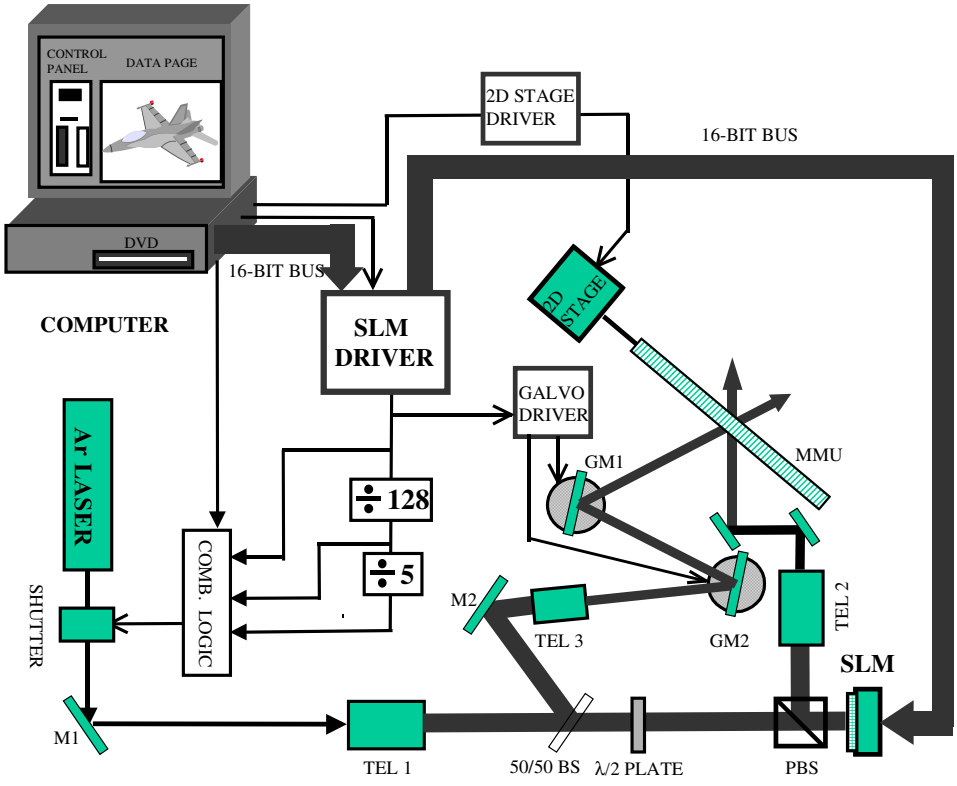

Figure 5. Schematic illustration of the writing set up for producing the image correlator.

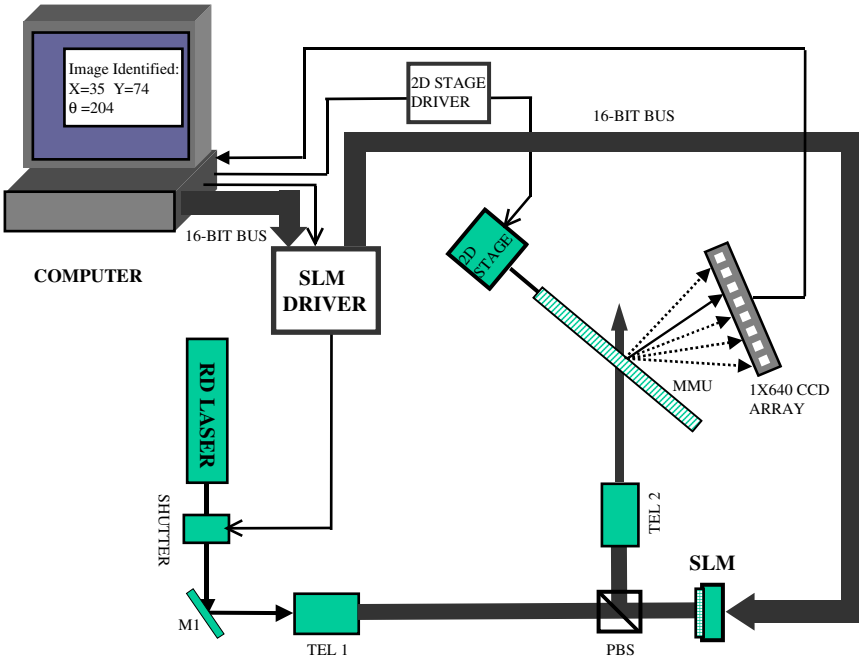

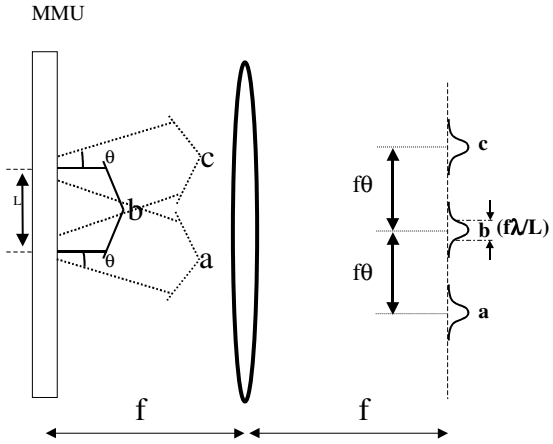

Figure 6. Top: Schematic illustration of the MMU based brass-board unit for image identification. Bottom: Lens to be inserted between the MMU and the CCD array in order to resolve the correlation spots. See text for details.

The reading process is illustrated in figure 6. The read-out is performed by a solid-state green laser (532 nm), with an output power of 20 mW. The output of this laser is passed through a shutter, and then expanded by a telescope (TEL1) to fill the area of the SLM. To start with, the image in question is loaded into the SLM driver. The image reflected from the SLM is redirected by the polarizing beam splitter (PBS), and reduced in size (TEL2) to match the area of the memory sub-unit.

In order to detect a possible correlation peak, a linear ccd array is placed 10 cm behind the MMU. A lens of focal length 5 cm is placed between the MMU and the ccd array, as shown in the bottom

of figure 6. Simple analysis then shows that the spots would be separated by a distance given approximately by $f\theta=25$ micron. The width of each spot is given approximately by $f\lambda/L$. The criterion for resolving the spots is then $L>\lambda/\theta$, which is clearly satisfied in our choice of parameters (L=2 mm, $\lambda/\theta \approx 1.06$ mm). Here we have assumed that the sidebands of the correlation peaks can be ignored; this can be guaranteed by making sure that the reference beams during the writing stage are not of square profile, but rather have Gaussian profiles. The ccd array consists of 640 elements, spaced 25 microns apart, in order to match the geometry chosen here.

Before the start of the query, the intensity of the read-out beam will be calibrated so that the correlation signal for a reference image produces an output voltage corresponding to a logic 1 for a TTL element. The 640 analog outputs will be loaded in parallel into a cascaded array of 20 shift-registers, each with 32 bits. Once the output signals are loaded into the registers, 640 cycles of a clock signal will be used to push the information out of the shift registers. The last (output) bit of the shift-register-cascade will be ANDed with a logic 1. The output of this AND gate will trigger the loading of a %640 counter (also driven by the same clock) into an 11 bit register, which in turn will be loaded into the computer through its parallel port. It is plausible that more than one correlation corresponding to a TTL logic 1 will occur. In this case, the power of the read-out beam will be reduced by a pre-determined amount, and the process repeated, until only one of the correlation peak registers as a logic 1. If no correlation occurs, the shutter is turned off, the 2D stage is moved to the next location, and the shift-registers are scanned again. This process is to be repeated through all the positions of the 2D Stage until a correlation peak is found.